

# Influence of Tibetan Plateau On The North American Summer Monsoon Precipitation

Qin Wen (✉ [wenq@pku.edu.cn](mailto:wenq@pku.edu.cn))

Nanjing Normal University <https://orcid.org/0000-0003-0858-3864>

Zixuan Han

Hohai University

Hajun Yang

Fudan University

Jianbo Cheng

Yancheng Institute of Technology

Zhengyu Liu

Ohio State University

Jian Liu

Nanjing Normal University

---

## Research Article

**Keywords:** Tibetan Plateau, North American summer monsoon, Hadley circulation, Atlantic meridional overturning circulation, Intertropical Convergence Zone

**Posted Date:** March 12th, 2021

**DOI:** <https://doi.org/10.21203/rs.3.rs-264225/v1>

**License:**  This work is licensed under a Creative Commons Attribution 4.0 International License.

[Read Full License](#)

---

1  
2 **Influence of Tibetan Plateau on the North American Summer Monsoon**  
3 **Precipitation**  
4

5  
6 Qin Wen\*<sup>1,2</sup>, Zixuan Han<sup>3</sup>, Hajun Yang<sup>4</sup>, Jianbo Cheng<sup>5</sup>, Zhengyu Liu<sup>6</sup>, Jian Liu<sup>1,2,7</sup>

7 <sup>1</sup>*School of Geography, Nanjing Normal University, Nanjing, 210023, China; Key Laboratory of Virtual*  
8 *Geographic Environment (Nanjing Normal University), Ministry of Education, Nanjing, 210023,*  
9 *China; Jiangsu Center for Collaborative Innovation in Geographical Information Resource*  
10 *Development and Application, Nanjing, 210023, China*

11 <sup>2</sup>*Open studio for Ocean-Climate-Isotope Modeling, Pilot National Laboratory for Marine Science and*  
12 *Technology (Qingdao), Qingdao, 266100, China*

13 <sup>3</sup>*College of Oceanography/Key Laboratory of Marine Hazards Forecasting, Ministry of Natural*  
14 *Resources/Key Laboratory of Ministry of Education for Coastal Disaster and Protection, Hohai*  
15 *University, Nanjing, 210024, China*

16 <sup>4</sup>*Department of Atmospheric and Oceanic Sciences, Institute of Atmospheric Science and CMA-FDU*  
17 *Joint Laboratory of Marine Meteorology, Fudan University, Shanghai, 200438, China*

18 <sup>5</sup>*School of Environmental Science and Engineering, Yancheng Institute of Technology, Yancheng*  
19 *224051, China*

20 <sup>6</sup>*Department of Geography, Ohio State University, USA*

21 <sup>7</sup>*Jiangsu Provincial Key Laboratory for Numerical Simulation of Large Scale Complex Systems, School*  
22 *of Mathematical Science, Nanjing Normal University, Nanjing 210023, China*  
23 *Climate of Dynamics*

24 Submitted, March 11, 2021

25        \**Corresponding author address*: Qin Wen, School of Geography, Nanjing Normal University,  
26                Nanjing, China, 210023.  
27        Email: [wenq@pku.edu.cn](mailto:wenq@pku.edu.cn)

28

**Abstract**

29 It has been well known that the uplift of the Tibetan Plateau (TP) can significantly enhance the  
30 Asian monsoon. Here, by comparing the sensitivity experiments with vs without the TP, we find that  
31 TP uplift can also increase the precipitation of North American Summer Monsoon (NASM), with  
32 atmosphere teleconnection accounting for 6% and oceanic dynamical process accounting for another  
33 6%. Physically, TP uplift generates a stationary Rossby wave train traveling from Asian continent to  
34 the North Atlantic region, resulting in an anomalous high-pressure over tropical-subtropical North  
35 Atlantic. The anomalous subtropical high enhances the low level southerly winds, forcing an  
36 anomalous upward motion over North American monsoon (NAM) region and then an increased  
37 summer precipitation there. In addition, TP uplift enhances the Atlantic meridional overturning  
38 circulation, which reduces the meridional temperature gradient and leads to a northward shift of  
39 Hadley Cell over eastern Pacific-Atlantic section. The latter shifts the convection center northward to  
40 10°N and further increases the NASM precipitation. The enhanced NASM precipitation can also be  
41 understood by the northward shift of Intertropical Convergence Zone. Our study implies that the  
42 changes of NAM climate can be affected by not only local process but also remote forcing, including  
43 the Asian highland.

44

45

46

47 **Keywords** Tibetan Plateau · North American summer monsoon · Hadley circulation · Atlantic  
48 meridional overturning circulation · Intertropical Convergence Zone

## 49 **1. Introduction**

50 The uplift of the Tibetan Plateau (TP) has been known to generate a great impact on regional  
51 climate change, especially for monsoon climate, although the precise history of the TP uplift is still  
52 controversial (Harrison et al., 1992; An, 2001; Molnar et al., 2010). For example, the monsoon intensity  
53 over South Asian shows a correlation with the rate of Himalayan exhumation over the past 23 Myr  
54 (Million years) (Clift, 2008). The enhanced southwesterly winds, documented by the planktonic  
55 foraminifer over Arabian Sea, indicating the strengthening of Indian summer monsoon about 9-8 Myr  
56 ago (Kroon et al., 1991; Prell et al., 1992, 1997). New basal dates from the aeolian “Red Clay”  
57 sediments on the Chinese Loess plateau indicate onset of aeolian dust accumulation at about 7.6 Myr  
58 ago (An et al., 2001). The change in oxygen isotope composition of soil carbonates in Pakistan infers  
59 changes in vegetation from forests to grasses in Pakistan beginning about 8 Myr ago (Quade et al.,  
60 1989), and a change from mixed needle-leaf or broad-leaf forests to grassland vegetation along the  
61 northeastern margin of the TP about 8.5 Myr ago (Cerling et al., 1997), which indicates increased  
62 summer precipitation.

63 Until now, the TP uplift on Asian monsoon has been studied extensively. Several studies  
64 investigate the Asian summer monsoon behavior under the TP elevation forcing (Boos and Kuang,  
65 2010; Park et al., 2012; Wu et al., 2012). Major results were that the uplift of the TP significantly  
66 increases the Asian monsoon intensity (Prell and Kutzbach, 1992) and variability (Fallah et al., 2016).  
67 Considering different stages of TP uplift, Jiang et al (2008), as well as Liu and Yin (2002) find that an  
68 East Asian summer monsoon system similar to that of the present initially exists when the TP uplift 60%  
69 of its modern height and is gradually intensified with the continued plateau uplift. An et al. (2001)  
70 confirm the linkage of stages in evolution of Asian monsoons to the phases of the Himalaya-Tibetan  
71 plateau uplift. In addition, the uplift of different parts of the TP on distinct Asian monsoon climate has  
72 also been verified by recent numerical experiments (Zhang et al., 2010; Tang et al., 2013). Boos and  
73 Kuang (2010) reveal that the large-scale South Asian summer monsoon circulation is unaffected by

74 removal of the plateau, instead, it depends on the exists of narrow orography of the Himalayas and  
75 adjacent mountain. This has also been confirmed by Wu et al (2012), in which they suggest that the  
76 mechanical effect of the plateau is not the major driver of the Asian summer monsoon.

77 However, few studies have focused on the impact of the TP topography on North American  
78 monsoon (NAM) climate. Dominated by perennially dry conditions, the NAM contributes  
79 approximately 40 and 70% of the annual total precipitation for the southwest United States and  
80 northwest Mexico, respectively (Higgins et al., 1997). The NAM is associated with anomalous  
81 westerlies to the southwest of the anomalous cyclone transporting water vapor from the eastern tropical  
82 Pacific and the Gulf of California, characterized by a local cyclonic anomaly with distinct rainfall  
83 maxima over western Mexico (Yim et al., 2014).

84 The motivation for this study is that, contrast to Asian monsoon region located to the west of the  
85 Pacific Ocean, the NAM region is located over eastern Pacific Ocean and close to Atlantic Ocean.  
86 Some works suggest an intercontinental contrasting precipitation anomaly between Asia and North  
87 America, that is, the extensive precipitation increase over Asian monsoon regions always accompanies  
88 with droughts over North America (Zhao et al., 2016). So, we wonder if the TP uplift could generate  
89 this feature since the TP uplift produces massive summer precipitation increase over Asian monsoon  
90 region. In addition, previous works demonstrate that the negative SST anomalies in the North Atlantic  
91 can substantially alter the North Atlantic subtropical high, which may ultimately influence the NAM  
92 (Kushnir et al., 2010; Parsons et al., 2014; Wang et al., 2014). The NAM is also closely linked to  
93 tropical Pacific sea surface temperature (Castro et al., 2001). The positive temperature anomaly over  
94 eastern-central Pacific can displace the North Pacific intertropical convergence zone and the South  
95 Pacific convergence zone equatorward, thereby directly reducing the NAM rainfall (Webster et al.,  
96 1998; Wang et al., 2012).

97 Our previous works suggest that the TP uplift may enhance the trade winds over the Pacific Ocean  
98 and the establishment of the Atlantic meridional overturning circulation (Wen and Yang, 2020; Yang

99 and Wen, 2020). How would the North American summer monsoon (NASM) precipitation may change  
100 under the TP uplift? This question has rarely been addressed in previous works. Here, we will examine  
101 the evolution of the NASM and its mechanisms by checking the atmospheric process and oceanic  
102 feedbacks, which has never been addressed before.

103 This paper is arranged as follows. An introduction to the model and experiments, as well as the  
104 methods is given in section 2. Changes in mean climate and NASM precipitation are illustrated in  
105 section 3. Mechanisms for NASM precipitation change are analyzed in section 4. Summary and  
106 discussion are given in section 5.

## 107 **2. Model and methods**

### 108 2.1 Model and experiments

109 The Community Earth System Model (CESM1.0) is applied in this study. This model has been  
110 widely used to study the Earth's past, present, and future climate states (<http://www2.cesm.ucar.edu/>).  
111 CESM was developed by the U.S. National Centre for Atmospheric Research (NCAR) and is  
112 composed of atmosphere model (Community Atmosphere Model; CAM5), ocean model (Parallel  
113 Ocean Program; POP2), land surface model (Community Land Model; CLM4), sea ice model  
114 (Community Ice Code; CICE4) components and one coupler (CPL7). Detailed model descriptions can  
115 be found in Wen and Yang (2020).

116 To detailly assess the TP uplift on NASM precipitation, we separate the atmospheric and  
117 oceanic dynamical process by conducting two groups of simulations using CESM low resolution  
118 (T31\_g37) configuration. The first group is fully coupled run, including a 2400-year real simulation  
119 and a 400-year no-mountain run. The real simulation is named "CTRL", in which the model  
120 geometry, topography, and continents are realistic (Fig. 1a). The CTRL run reaches equilibrium state  
121 around 2000 years (Yang et al. 2015). The sensitive run (named "NoTP") starts from the year 2001 of

122 CTRL, and is integrated for 400 years with the topography around the TP set to 50m above the sea  
123 level (Fig. 1b). Except the topography elevation, all other boundary conditions, such as vegetation and  
124 albedo remain unmodified and they are free adjusted. The second group is slab ocean (SOM) run, in  
125 which the ocean dynamical process has been shut-down and replaced by a mixed layer from the  
126 climatology of CTRL simulation. Two experiments in this group are named “CTRL\_SOM” and  
127 “NoTP\_SOM”, in which the topography is set as that in “CTRL” and “NoTP”, respectively.  
128 “CTRL\_SOM” is integrated for 400 years and “NoTP\_SOM” starts from the year 201 of  
129 “CTRL\_SOM” and is integrated for 200 years. The equilibrium changes are deduced by using data  
130 from the last 100 years of each experiments. The difference between the “CTRL” and “NoTP” is for  
131 the sum of atmospheric and oceanic dynamical process, and the difference between the  
132 “CTRL\_SOM” and “NoTP\_SOM” can be treated as atmospheric effect.

## 133 2.2 North American monsoon region

134 According to Wang and Ding (2008), the NAM domain is delineated by the region in which the  
135 local summer precipitation minus local winter precipitation exceeding 2mm/day and the local summer  
136 precipitation exceeds 55% of annual rainfall. Based on this definition, the NAM regions are clearly  
137 shown in Fig. 3d by using the GPCP data (outlined by purple contours). The monsoon regions  
138 obtained by CESM CTRL simulation are similar to the GPCP’s results (outlined by black contours),  
139 which is also shown in Liu et al (2016). The NAM domain obtained in this study is primarily based  
140 on precipitation contrast in the solstice seasons and is larger than that traditionally recognized by  
141 many scientists working on the NAM (Wang et al., 2021). The NASM precipitation can be obtained  
142 by the weighted-area average local summer precipitation over the NAM area.

## 143 2.3 Moisture budget

144 To reveal the mechanisms that govern changes in NASM precipitation related to the TP uplift,  
 145 we analyse changes in the moisture budget according to Chou et al. (2009):

$$146 \quad P' = E' - \bar{\omega} \frac{\partial q'}{\partial p} - \omega' \frac{\partial \bar{q}}{\partial p} - \langle \bar{V} \cdot \nabla q' \rangle - \langle V' \cdot \nabla \bar{q} \rangle + R \quad (1)$$

147 Here,  $P$  is precipitation,  $E$  is surface evaporation,  $\omega$  is vertical velocity,  $q$  is specific  
 148 humidity,  $p$  is pressure,  $V$  is horizontal wind vector,  $R$  is residual. Overbars represent monthly  
 149 means in CTRL, and primes denote the difference between CTRL and NoTP. Based on this equation,  
 150 the monsoon precipitation change can be decomposed into evaporation change ( $E'$ ), the  
 151 thermodynamic and dynamic changes of vertical moisture advection ( $-\bar{\omega} \frac{\partial q'}{\partial p}$  and  $-\omega' \frac{\partial \bar{q}}{\partial p}$ ), and  
 152 thermodynamic and dynamic changes of horizontal moisture advection ( $-\langle \bar{V} \cdot \nabla q' \rangle$  and  $-\langle V' \cdot \nabla \bar{q} \rangle$ )  
 153 and the residual  $R$ .

#### 154 2.4 Three-pattern decomposition of global atmospheric circulation

155 The monsoon circulation is the component of large-scale atmospheric motion. The large-scale  
 156 atmospheric motion to first order is consist of Rossby wave at mid-high latitudes (Rossby, 1939),  
 157 Hadley and Walker circulation at low latitudes (Trenberth and Solomon, 1994; Julian and Chervin,  
 158 1978). However, these components interact with each other and is hard to be distinguished in the real  
 159 world. Fortunately, a new method named the three-pattern decomposition of global atmospheric  
 160 circulation (3P-DGAC) has been introduced by Hu et al (2017), by which the global atmospheric  
 161 circulation  $\vec{V}$  is decomposed into the horizontal circulation ( $\vec{V}'_R$ ), meridional circulation ( $\vec{V}'_H$ ) and  
 162 zonal circulation ( $\vec{V}'_W$ ) as follows,

$$163 \quad \vec{V}' = \vec{V}'_H + \vec{V}'_W + \vec{V}'_R \quad (2)$$

164 in which,

$$165 \quad \begin{cases} \vec{V}'_R(\lambda, \theta, \sigma) = u'_R(\lambda, \theta, \sigma)\vec{i} + v'_R(\lambda, \theta, \sigma)\vec{j} \\ \vec{V}'_H(\lambda, \theta, \sigma) = v'_H(\lambda, \theta, \sigma)\vec{j} + \dot{\sigma}_H(\lambda, \theta, \sigma)\vec{k} \\ \vec{V}'_W(\lambda, \theta, \sigma) = u'_W(\lambda, \theta, \sigma)\vec{i} + \dot{\sigma}_W(\lambda, \theta, \sigma)\vec{k} \end{cases} \quad (3)$$

$$166 \quad \begin{cases} u'_R = -\frac{\partial R}{\partial \theta}, v'_R = \frac{1}{\sin\theta} \frac{\partial R}{\partial \lambda} \\ v'_H = -\frac{\partial H}{\partial \sigma}, \dot{\sigma}_H = \frac{1}{\sin\theta} \frac{\partial(\sin\theta H)}{\partial \theta} \\ u'_W = \frac{\partial W}{\partial \sigma}, \dot{\sigma}_W = -\frac{1}{\sin\theta} \frac{\partial W}{\partial \lambda} \end{cases} \quad (4)$$

167 Where  $(\lambda, \theta, \sigma)$  is the spherical  $\sigma$ -coordinate system,  $(u'_R, v'_R)$ ,  $(v'_H, \dot{\sigma}_H)$  and  $(u'_W, \dot{\sigma}_W)$  are the wind  
 168 vector components of horizontal circulation, meridional circulation, and zonal circulation,  
 169 respectively.  $R$ ,  $H$ , and  $W$  are the stream functions which can be obtained from following equation:

$$170 \quad \Delta_3 R = \zeta \quad (5)$$

$$171 \quad \frac{\partial H}{\partial \sigma} = \frac{1}{\sin\theta} \frac{\partial R}{\partial \lambda} - v' \quad (6)$$

$$172 \quad \frac{\partial W}{\partial \sigma} = \frac{\partial R}{\partial \theta} + u' \quad (7)$$

173 Where  $\Delta_3 = \frac{1}{\sin^2\theta} \frac{\partial^2}{\partial \lambda^2} + \frac{1}{\sin\theta} \frac{\partial}{\partial \theta} \left( \sin\theta \frac{\partial}{\partial \theta} \right) + \frac{\partial^2}{\partial \sigma^2}$  is the three-dimensional Laplacian in the  
 174 spherical  $\sigma$ -coordinates and  $\zeta = \frac{1}{\sin\theta} \frac{\partial v'}{\partial \lambda} - \frac{1}{\sin\theta} \frac{\partial(u' \sin\theta)}{\partial \theta}$  is the vertical vorticity of the entire  
 175 atmospheric layer.  $(u', v', \dot{\sigma})$  represent the three velocity components in the spherical  $\sigma$ -coordinate  
 176 system.

### 177 3. Changes in mean climate and NASM precipitation

178 To better understand the response of NASM precipitation to the TP uplift, the mean climate  
 179 change are firstly examined here. The TP uplift immediately induces anticyclonic geopotential height  
 180 anomalies to the north of the TP area and over the tropical-subtropical North Atlantic, and cyclonic  
 181 anomalies to the south of the TP area, extending to subpolar Pacific and subpolar Atlantic (Fig. 2b).  
 182 The atmospheric circulation changes are roughly barotropic since the wave pattern at 500 hPa shows

183 resemblance to that at 850 hPa (Yang and Wen, 2020). The adjustment of planetary wave pattern is  
184 very fast and is also confirmed by our CAM5 model simulation (Figure not shown). More importantly,  
185 the atmospheric responses do not change much from SOM runs to fully coupled runs (Fig. 2b vs 2d),  
186 indicating that the oceanic dynamical process in the hundreds of years latter do not have considerable  
187 feedback to the atmospheric circulation. Detailed atmospheric circulation changes are also discussed  
188 in Yang et al (2020), which states that the teleconnection patterns in Fig. 2a and Fig. 2d agree well  
189 with those in previous studies (Zhao et al., 2007, 2012) and can be well understood by the classic  
190 planetary wave theory in a linear quasigeostrophic system (Hoskins and Karoly, 1981).

191       The anomalous high pressure over the tropical-subtropical North Atlantic strengthens the trade  
192 winds over the tropical eastern Pacific-Atlantic section, which promotes the surface sensible heat loss  
193 (Figure not shown) and results in cold surface air temperature (SAT) anomaly in SOM runs (Fig. 2c).  
194 In fully coupled runs, the strengthened trade winds over the tropical eastern Pacific-Atlantic section  
195 can brings the cold subsurface water upward and further cools the SAT (Fig. 2e). In addition, the  
196 uplift of the TP can also lead to the establishment of the AMOC (Fig. 2a) by inducing more water  
197 vapor transport from the North Atlantic to Pacific Ocean (Yang and Wen, 2020). The establishment  
198 of the AMOC warms the North Atlantic by generating pronounced heat transport from Southern  
199 Hemisphere (SH) to Northern Hemisphere (NH) (Fig. 2e).

200       The time evolution of changes in NASM precipitation under the TP uplift are shown in Fig. 3a.  
201 The TP uplift immediately results in NASM precipitation increase by 0.5 mm/day (6%). This can be  
202 seen from the SOM runs (light blue curve) or the fully coupled runs during the first several decades  
203 (blue curve) when the oceanic dynamical process is not fully responded. The oceanic dynamical  
204 feedback further doubles the NASM precipitation change and leads to precipitation increase to 0.9  
205 mm/day (12%). The spatial distribution of monsoon precipitation is shown in Fig. 3b and d. The

206 NAM region is characterized by a large extent of significant summer precipitation increase via  
207 atmospheric process (Fig. 3b) and is further amplified by oceanic dynamical feedback (Fig. 3d). It is  
208 interesting to note that the precipitation is consistently increased over the NAM region by  
209 atmospheric process (Fig. 3b) while the precipitation change induced by oceanic dynamical process  
210 exhibits an out-of-phase pattern with large precipitation increase occurred over central to north NAM  
211 region and decrease over south NAM region (Fig. 3d). The changes in surface humidity are also  
212 checked here (Fig. 3c and e). The surface air humidity is slightly increased over NAM region in SOM  
213 runs (Fig. 3c). In fully coupled runs, the surface air humidity change over NAM region shows a  
214 similar pattern to precipitation change, with increase over central to north NAM region and decrease  
215 over south NAM region (Fig. 3e). In this study, the temperature is decreased over NAM region (Fig.  
216 2c and e). Usually, the surface air cooling can suppress the convection and result in less precipitation  
217 (Xie et al., 2010), followed by drier air. The inconsistency between surface air temperature and  
218 precipitation (humidity) change here indicates that the thermal process may not important in shaping  
219 the final precipitation and humidity change.

## 220 **4. Mechanisms for NASM precipitation change**

### 221 4.1 Moisture budget

222 To understand the processes that drive the NASM precipitation change, the projected changes in  
223 precipitation and the first five terms on the right-hand side of Eq. (1) are shown in Fig. 4 and Fig. 5.  
224 Note that since we use 100-year data, all variables with color shadings are exceeding 95% confidence  
225 level determined by a two-tailed Student's t test. For simplifying the figure, we do not add stippling  
226 anymore. It is obvious that the dynamic change of vertical moisture advection is the largest  
227 contributor to the increased NASM precipitation both in SOM runs and fully coupled runs, with the  
228 magnitude in fully coupled runs much bigger than that in SOM runs (Fig. 4d and Fig. 5d). The

229 enhanced vertical moisture advection is due to the increased upward motion, a point to be returned  
230 later. The evaporation term is hardly changed because the TP-uplift induced surface temperature  
231 change over this region is small (Fig. 2c and e). The weak temperature change also contributes to the  
232 hardly changed thermodynamic component of vertical moisture advection (Fig. 4c and Fig. 5c). The  
233 thermodynamic and dynamic changes in horizontal moisture advection are both uncertain and small  
234 over NAM region (Fig. 4e, f and Fig. 5e, f), consistent with previous studies that the horizontal  
235 moisture advection is usually less important than vertical moisture advection to precipitation (Chou et  
236 al., 2009; Zhang et al., 2017). The contribution of these terms to NASM precipitation change are  
237 summarized in Fig. 6a. The dynamic change of vertical moisture advection term nearly contributes  
238 100% precipitation increase in SOM runs and fully coupled runs, respectively, which is undoubtable  
239 the dominant term for NASM precipitation change. Based on Eq. (2)-Eq. (7), the dynamic change of  
240 vertical moisture advection term can be further break into vertical moisture advection due to  
241 meridional circulation and zonal circulation change (Fig. 6b). It is obvious that the increased dynamic  
242 change of vertical moisture advection term ( $-\langle\omega'q\rangle$ ) largely comes from meridional circulation  
243 change ( $-\langle\omega_H'q\rangle$ ). The zonal circulation change appears to suppress the NASM precipitation increase  
244 ( $-\langle\omega_W'q\rangle$ ).

#### 245 4.2 Mean vertical velocity and 3P-DGAC

246 To understand the atmospheric circulation change, the mean atmospheric vertical velocity are  
247 first shown in Fig. 7. In the annual mean state of observations, the large-scale upward motion is  
248 expected in the tropics, with centers near equatorial Africa, the Indian Ocean, the western Pacific, the  
249 eastern Pacific, the South America, and the Atlantic Ocean (Chen et al., 2014; Cheng et al., 2020).  
250 These features are also captured in our CTRL simulation (Fig. 7a). Strong upward motion in the  
251 tropics is associated with deep convection and corresponds to above-normal precipitation in these

252 regions while strong descending motion in the subtropics suppresses the convection and corresponds  
253 to the aridity (Chen et al., 2014). Thus, the equatorial Africa, the Indian Ocean, the western Pacific,  
254 the eastern Pacific, South America, and the Atlantic Ocean are characterized by a stronger  
255 precipitation than other regions (Fig. 8a). Compared to CTRL simulation, the CTRL\_SOM exhibits  
256 weakened upward motion (Fig. 7c), suggesting that the ocean dynamics are important for shaping the  
257 atmospheric convection. As a consequence, the precipitation is much lower in CTRL\_SOM compared  
258 with that in CTRL (Fig. 8c vs 8a). During boreal summer, the upward motion gets stronger in NH and  
259 weaker in SH (Fig. 7e-h compared with Fig. 7a-d), indicating the large scale shifts of Intertropical  
260 Convergence Zone (ITCZ) (Fig. 8e-h compared with Fig. 8a-d). Comparing CTRL\_SOM and  
261 NoTP\_SOM, the upward motion seems strengthened over NAM region (Fig. 7g and h), resulting in  
262 more precipitation over NAM region (Fig. 8g and h). Comparing CTRL and NoTP, the TP uplift  
263 leads to a northward shift of the maximum upward motion over NAM region (Fig. 7e and f),  
264 indicating a northward shift of maximum precipitation over this region (Fig. 8e and f).

265 Previous works suggest that the tropical overturning circulation consists of a couple of  
266 orthogonal overturning circulation, that is, meridional and zonal circulations (Hu et al., 2018). Based  
267 on 3P-DGAC method, the vertical wind can be decomposed into two parts, the vertical winds related  
268 to meridional circulation and zonal circulation. i.e.,  $\omega = \omega_H + \omega_W$ , where  $\omega$ ,  $\omega_H$  and  $\omega_W$   
269 represent the total vertical wind, the vertical wind of meridional circulation and that of zonal  
270 circulation, respectively (Hu et al., 2018). From Fig. 9b and f, we can see that the vertical wind of  
271 meridional component shares the identical center to total vertical wind (Fig. 9a vs b and Fig. 9e vs f),  
272 indicating the ascending branch of regional Hadley circulations (Cheng et al., 2020). All these  
273 regional Hadley circulations are characterized by two circulations with rising branch in the tropical  
274 regions and sinking branch in the subtropics of both hemispheres (Fig. 9b and f). For zonal circulation,  
275 there are three main centers over the Indian Ocean, the western Pacific Ocean and the western

276 Atlantic Ocean, representing the three rising branches of Walker circulation (Fig. 9c and g). The  
277 sinking branches of Walker circulation are located in the western Indian Ocean, the eastern Pacific  
278 Ocean and the eastern Atlantic Ocean (Hu et al., 2017). The residual term is very small and can be  
279 negligible in latter discussion (Fig. 9d and h). The decomposition of vertical velocity is identical to  
280 previous works (Hu et al., 2017; Cheng et al., 2020). By using this method, we can analyze the  
281 regional meridional circulation and zonal circulation. The traditional method to define the Hadley  
282 circulation is based on the zonal average, so the contribution of the zonal component vanishes [ $\omega_W =$   
283 0] and  $[\omega]$  contains only  $[\omega_H]$ . Thus, it is appropriate to use zonal averaged total vertical velocity to  
284 represent the Hadley circulation in the previous studies (Wen et al., 2018). However, it is incorrect to  
285 use regional total vertical velocity, i.e., the vertical wind between 80°W and 10°W to represent the  
286 regional Hadley circulation since the  $\omega_W$  is not zero (Fig. 9c and g). In addition, the traditional  
287 definition of the Walker circulation is restricted to the tropical region and  $\langle \omega \rangle_{5^{\circ}S}^{5^{\circ}N}$  is often used to  
288 calculate the Walker circulation. In this case, the  $\langle \omega_H \rangle_{5^{\circ}S}^{5^{\circ}N} \neq 0$  (Fig. 7b and f), which means that the  
289 contribution of the meridional circulation is included in the vertical velocity of the Walker circulation.  
290 So, when analyzing the meridional circulation (zonal circulation), the vertical wind of meridional  
291 component (zonal component) should be used.

#### 292 4.3 Mechanisms for NASM precipitation change

293 The changes in vertical velocity and its meridional component and zonal component during  
294 boreal summer are shown in Fig. 10 to illustrate the mechanisms that govern the NASM precipitation  
295 response. The NAM region is characterized by an anomalous ascending motion, which is dominated  
296 by the meridional circulation change both in SOM runs and fully coupled runs (Fig. 10b and e).  
297 However, as mentioned in Section 4.2, the mechanisms may be different. In SOM runs, the TP uplift  
298 generates anomalous upward motion of meridional component over NAM region and its surrounding

299 regions, which dominates the total vertical wind change (Fig. 10b) and results in increased NASM  
300 precipitation (Fig. 6b). Compared to SOM runs, the anomalous upward motion in fully coupled runs  
301 is located further north with abnormal descending motion at the south tip of it, indicating that the  
302 meridional circulation shifts northward (Fig. 10e). The changes in upward motion of zonal component  
303 over NAM region is very small and uncertain compared with that of meridional component.

#### 304 4.3.1 Mechanisms in SOM runs: The atmospheric teleconnection response

305 The change in meridional component of vertical velocity over NAM region refers to the regional  
306 Hadley circulation (HC) response. Here, we define the regional HC over eastern Pacific-Atlantic  
307 sector as spanning 120°W-20°W (red box in Fig. 10b and e) and plot it in Fig. 11. In SOM runs, the  
308 summer HC gets strengthened in both hemispheres under the TP uplift with the magnitude in NH  
309 much stronger than that in SH (Fig. 11a). The strengthened HC in NH results in enhanced convection  
310 over NAM region and thus the increased summer precipitation (Fig. 6b). The strengthened regional  
311 HC in SOM runs is related to the adjustment of planetary waves (Fig. 2b). The anomalous positive  
312 geopotential height over tropical-subtropical North Atlantic is accompanied by the northeasterly wind  
313 at the south tip of it, which results in stronger regional HC over NAM region by enhancing the  
314 horizontal momentum flux from the surface into the atmosphere (Cook et al., 2003). Actually, the  
315 negative-positive geopotential anomaly over the North Atlantic is not unlike the positive phase of the  
316 North Atlantic oscillation, which is always associated with the enhanced HC (Wang et al., 2004;  
317 Cook et al., 2003; Iqbal et al., 2019).

#### 318 4.3.2 Mechanisms in fully coupled runs: The indirect impact from the altered AMOC

319 In fully coupled runs, the TP uplift induces a northward shift of HC in NH, resulting in increased  
320 upward motion over the NAM region (Fig. 11c and d). The northward shift of HC in fully coupled

321 runs can be understood by the meridional temperature gradient change. The uplift of the TP induces  
322 the establishment of AMOC (Fig. 2a), which brings substantial heat northward to warms the NH,  
323 especially over the North Atlantic. The profound warming over mid-high latitudes reduces the  
324 meridional temperature gradient, which leads to a northward shift of HC (Bush and Philander, 1999;  
325 Yang et al., 2017; D'Agostino et al., 2017; Liu and Zhou, 2017). Actually, there is close coupling  
326 between sea surface temperature and precipitation in the tropics (Xie et al., 2010). Over the eastern  
327 Pacific-Atlantic section in fully coupled runs, the SST warming is occurred north of 10°N while  
328 cooling is occurred south of 10°N (Fig. 12c). The asymmetric SST change and thus the weakened  
329 meridional temperature gradient lead to a profound upward motion around 10°N in the real world  
330 (Fig. 7e), otherwise the upward motion is located further south (Fig. 7f). This is consistent with the  
331 northward shift of precipitation (Fig. 12c). However, in SOM runs, the meridional temperature  
332 change is relatively small, so the HC hardly shifts.

333 The northward shift of precipitation in fully coupled runs can also be understood by regional  
334 ITCZ shift. The ITCZ position are shown in Fig. 12. For eastern Pacific-Atlantic section, the mean  
335 position of ITCZ in CTRL\_SOM, NoTP\_SOM, CTRL and NoTP during boreal summer are at 6.65°N,  
336 6.70°N, 5.91°N and 3.47°N, respectively. Thus, there is nearly no shift of ITCZ in SOM runs while  
337 the ITCZ shifts northward by 2.44°N in fully coupled runs under the TP uplift. The northward shift of  
338 ITCZ in fully coupled runs results in substantially precipitation increase over central to north NAM  
339 region and decrease over the south tip of NAM region (Fig. 12d). The northward shift of ITCZ over  
340 the eastern Pacific-Atlantic section is related to regional atmospheric energy budget (Boos and Korty,  
341 2016; Lintner and Boos, 2019). The energy input into atmosphere is shown in Fig. 13. In fully  
342 coupled runs, the TP uplift causes the net energy gain of the atmosphere in the NH, especially over  
343 the North Atlantic (Fig. 13a). The increase of the net energy input into the atmosphere over the North  
344 Atlantic comes from both the top-of-atmosphere (TOA) and surface. In details, the energy gain at the

345 TOA over the North Atlantic mainly comes from the shortwave radiation. The establishment of the  
346 AMOC warms the North Atlantic, which reduces the low clouds and enable more shortwave can  
347 come into the atmosphere (Figure not shown). Meanwhile, the energy gain at the surface mainly  
348 comes from the increased longwave radiation and latent heat flux into atmosphere (Figure not shown).  
349 The profound warming over North Atlantic induced by AMOC allows more longwave radiation loss  
350 from ocean to atmosphere. The warming can also enhance the ocean surface evaporation and thus the  
351 latent heat flux into atmosphere. In contrast to the profound energy gain in NH, the SH exhibits an  
352 energy loss since the setup of AMOC can generate bipolar seesaw phenomenon with warming in the  
353 NH and cooling in the SH. The South Ocean cooling leads to more sensible and latent heat flux  
354 transport from atmosphere to ocean, which results in energy loss in the SH (Figure not shown). The  
355 inter-hemispheric energy asymmetry over eastern Pacific-Atlantic section results in an increase of  
356 southward atmospheric energy transport occurred over the tropics (Fig. 13d), which is consistent with  
357 the revealed northward shift of the ITCZ (Fig. 12d). In addition, the atmospheric energy transport  
358 over tropics largely depends on the mean circulation change, i.e., the HC. Thus, the anomalous  
359 southward energy transport is completed by the northward shift the HC (Fig. 11c). On the contrary,  
360 the inter-hemispheric energy asymmetry is very small in SOM runs and the HC hardly shifts.

## 361 **5. Summary and discussion**

362 In this study, the impact of TP topography on NASM precipitation is investigated in SOM runs  
363 and fully coupled runs. TP uplift is found to enhance the NASM both directly via the atmospheric  
364 teleconnection and indirectly via the impact of the altered AMOC. First, the TP uplift alters the  
365 planetary wave patterns and generate enhanced Atlantic subtropical high, which strengthens the  
366 north-easterly wind over tropical eastern Pacific-Atlantic section and thus the enhanced regional HC  
367 there. The strengthened upward motion leads to enhanced convection and thus the increased NASM

368 precipitation. These processes are completed within several decades due to atmospheric adjustment.  
369 Second, the TP uplift can also enhance the NASM rainfall indirectly by first enhancing the AMOC,  
370 which reduces the meridional temperature gradient, leading to a northward shift of the HC. The  
371 northward shift of the HC shifts the center of the ascending motion northward to 10°N and  
372 substantially enhance the convection over the NAM region, and then, the NASM precipitation. This  
373 study shows a robust relationship between the topography of the TP and NASM precipitation,  
374 complimentary to previous perspective that TP uplift can substantially change rainfall over the Asian  
375 monsoon region.

376 The topography of the TP in shaping the NASM precipitation is helpful for our understanding of  
377 the TP's role in the global climate system. Previous studies mostly focus on the TP impact on Asian  
378 monsoon precipitation, while we highlight the connection between the TP topography and North  
379 American monsoon precipitation and show that the existence of the TP leads to more humid NAM  
380 climate. The results obtained in this study may be model dependent. For example, the horizontal  
381 resolution is reported to be crucial for adequately representing the NAM by accurately resolve the  
382 summertime low-level flow along the Gulf of California (Pascale et al., 2019). The NAM is also  
383 affected by SST biases. The excessive cold tongue is a common feature in general circulation model  
384 (Wen et al., 2020), which may alter the response of NASM precipitation to TP uplift. Although this is  
385 a highly idealized modeling study with some model limitations, this work helps explain the  
386 quantitative role of the TP in the real world. The evolution of tropical American climate during the  
387 geological time period is not only related to regional circulation change, but also links to Asian high  
388 land regions.

389 Our modeling results may have applications for paleoclimate study. For example, previous  
390 works use fossil flowers to reconstruct the Miocene climate over south Mexico and show that the

391 environmental conditions of the Chiapas is warmer and drier than in the present (Hernández et al.,  
392 2020), which is consistent with our study. Su et al (2018) use climate models and show that water  
393 vapor is divergent over tropical American continent without the TP, indicating that the tropical  
394 American continent is much drier in a world without the TP. Huber and Goldner (2012) analyze the  
395 Eocene monsoons and show that a high TP can generate precipitation over central American region,  
396 consistent with this study. As suggested in previous works, the elevated TP heating can affect the  
397 Asian-Pacific Oscillation intensity, with positive anomalies of tropospheric temperature deviation  
398 over the Eurasian continent and negative anomalies of tropospheric temperature deviation over the  
399 central and eastern North Pacific, as well as the Atlantic Ocean (Nan et al., 2009; Duan et al., 2012).  
400 The teleconnection pattern is also found in our studies.

401 This work may also have some implications on modern climate. The TP uplift can induce  
402 thermal heating at middle troposphere by lapse rate relationship, which shows resemblance to the  
403 rapid warming over the TP in the past decades (Duan and Xiao, 2015). There are many studies show  
404 that the TP heating could enhance East Asian summer rainfall (Wang et al., 2008), the monsoon  
405 rainfall variability in Pakistan (Wang et al., 2019), more studies should focus on the climate change  
406 outside the Asian continent, i.e., the North American and North Atlantic to highlight the importance  
407 of TP in shaping the global climate.

408 *Acknowledgement:* This work is supported by the NSF of China (Nos. 91737204, 41725021,  
409 41376007, 41630527 and 4201101394) and the Fundamental Research Funds for the Central  
410 Universities: B210201009. The experiments were performed on the supercomputers at the Chinese  
411 National Supercomputer Centre in Tianjin (Tian-He No. 1).

412

## References

- 413 An, Z., J. Kutzbach, W. Prell, et al., 2001: Evolution of Asian monsoons and phased uplift of the  
414 Himalaya-Tibetan plateau since Late Miocene times. *Nature*, **411**(6833): 62-66.
- 415 Boos, W. R., Z. Kuang, 2010: Dominant control of the South Asian monsoon by orographic insulation  
416 versus plateau heating. *Nature*, **463**(7278): 218-222.
- 417 Boos, W. R., R. L. Korty, 2016: Regional energy budget control of the intertropical convergence zone  
418 and application to mid-Holocene rainfall. *Nature Geoscience*, **9**(12): 892-897.
- 419 Bush, A. B. G., S. G. H. Philander, 1999: The climate of the Last Glacial Maximum: Results from a  
420 coupled atmosphere-ocean general circulation model. *Journal of Geophysical Research:*  
421 *Atmospheres*, **104**(D20): 24509-24525.
- 422 Castro, C. L., T. B. McKee, Sr. R. A. Pielke, 2001: The relationship of the North American monsoon to  
423 tropical and North Pacific sea surface temperatures as revealed by observational analyses. *J. Clim.*,  
424 **14**(24): 4449-4473.
- 425 Chen, S., K. Wei, W. Chen, et al., 2014: Regional changes in the annual mean Hadley circulation in  
426 recent decades. *Journal of Geophysical Research: Atmospheres*, **119**(13): 7815-7832.
- 427 Cheng, J., S. Hu, C. Gao, et al., 2020: On the discrepancies in the changes in the annual mean Hadley  
428 circulation among different regions and between CMIP5 models and reanalyses. *Theoretical and*  
429 *Applied Climatology*, **141**(3): 1475-1491.
- 430 Chou, C., J. D. Neelin, C. A. Chen, and J. Y. Tu, 2009: Evaluating the “rich-get-richer” mechanism in  
431 tropical precipitation change under global warming. *J. Clim.*, **22**, 1982-2005.
- 432 Clift, P. D., 2008: Greater Himalayan exhumation triggered by Early Miocene monsoon intensification.  
433 *Nature Geoscience*.
- 434 Cook, K. H., 2003: Role of continents in driving the Hadley cells. *Journal of the atmospheric sciences*,  
435 **60**(7): 957-976.

- 436 D'Agostino, R., P. Lionello, O. Adam, et al., 2017: Factors controlling Hadley circulation changes from  
437 the Last Glacial Maximum to the end of the 21st century. *Geophysical Research Letters*, **44**(16):  
438 8585-8591.
- 439 Duan, A., G. Wu, Y. Liu, et al., 2012: Weather and climate effects of the Tibetan Plateau. *Advances in*  
440 *Atmospheric Sciences*, **29**(5): 978-992.
- 441 Duan, A. M., Z. X. Xiao, 2015: Does the Climate Warming Hiatus Exist Over the Tibetan Plateau? *Sci.*  
442 *Rep.*, **5**:13711.
- 443 de Jesús Hernández-Hernández, M., J. A. Cruz, C. Castañeda-Posadas, 2020: Paleoclimatic and  
444 Vegetation Reconstruction of the Miocene Southern Mexico using Fossil Flowers. *Journal of*  
445 *South American Earth Sciences*, **104**: 102827.
- 446 Fallah, B., U. Cubasch, K. Prömmel, et al., 2016: A numerical model study on the behaviour of Asian  
447 summer monsoon and AMOC due to orographic forcing of Tibetan Plateau. *Clim. Dyn.*, **47**(5):  
448 1485-1495.
- 449 Harrison, T. M., P. Copeland, W. S. F. Kidd, and A. Yin, 1992: Raising Tibet. *Science*, **255**, 1663-1670.
- 450 Higgins, R. W., Y. Yao, X. L. Wang, 1997: Influence of the North American monsoon system on the  
451 US summer precipitation regime. *J. Clim.*, **10**(10): 2600-2622.
- 452 Hoskins, B. J., and D. J. Karoly, 1981: The steady linear response of a spherical atmosphere to thermal  
453 and orographic forcing. *J. Atmos. Sci.*, **38**, 1179-1196.
- 454 Hu, S., J. Cheng, J. Chou, 2017: Novel three-pattern decomposition of global atmospheric circulation:  
455 generalization of traditional two-dimensional decomposition. *Clim. Dyn.*, **49**(9): 3573-3586.
- 456 Hu, S., J. Chou, J. Cheng, 2018: Three-pattern decomposition of global atmospheric circulation: part I  
457 — decomposition model and theorems. *Clim. Dyn.*, **50**(7): 2355-2368.
- 458 Huber, M., A. Goldner, 2012: Eocene monsoons. *Journal of Asian Earth Sciences*, **44**: 3-23.

- 459 Iqbal, M. J., S. U. Rehman, S. Hameed, et al., 2019: Changes in Hadley circulation: the Azores high and  
460 winter precipitation over tropical northeast Africa. *Theoretical and Applied Climatology*, **137**(3):  
461 2941-2948.
- 462 Jiang, D., Z. Ding, H. Drange, et al., 2008: Sensitivity of East Asian climate to the progressive uplift  
463 and expansion of the Tibetan Plateau under the mid-Pliocene boundary conditions. *Advances in*  
464 *Atmospheric Sciences*, **25**(5): 709-722.
- 465 Julian, P. R., R. M. Chervin, 1978: A study of the Southern Oscillation and Walker Circulation  
466 phenomenon. *Mon. Weather. Rev.*, **106**:1433-1451.
- 467 Kroon, D., T. Steens, and S. R. Troelstra, 1991: Onset of the monsoonal related upwelling in the  
468 western Arabian Sea as revealed by planktonic foraminifera, in Prell, W. L., et al., Proceedings of  
469 the Ocean Drilling Program, Scientific results, Volume 117: College Station, Texas, Ocean  
470 Drilling Program, p. 257-263.
- 471 Kushnir, Y., R. Seager, M. Ting, N. Naik, J. Nakamura, 2010: Mechanisms of tropical Atlantic SST  
472 influence on North American precipitation variability. *J. Clim.* **23**, 5610-5628.
- 473 Lintner, B. R., W. R. Boos, 2019: Using atmospheric energy transport to quantitatively constrain South  
474 Pacific convergence zone shifts during ENSO. *J. Clim.*, **32**(6): 1839-1855.
- 475 Liu, B., T. Zhou, 2017: Atmospheric footprint of the recent warming slowdown. *Scientific Reports*, **7**(1):  
476 1-7.
- 477 Liu, F., J. Chai, B. Wang, et al., 2016: Global monsoon precipitation responses to large volcanic  
478 eruptions. *Scientific Reports*, **6**(1): 1-11.
- 479 Liu, X., Z. Y. Yin, 2002: Sensitivity of East Asian monsoon climate to the uplift of the Tibetan Plateau.  
480 *Palaeogeography, Palaeoclimatology, Palaeoecology*, **183**(3-4): 223-245.
- 481 Mamalakis, A., J. T. Randerson, J. Y. Yu, et al., 2021: Zonally contrasting shifts of the tropical rain belt  
482 in response to climate change. *Nature Climate Change*, 1-9.
- 483

- 484 Molnar, P., W. Boos, D. Battisti, 2010: Orographic Controls on Climate and Paleoclimate of Asia:  
485 Thermal and Mechanical Roles for the Tibetan Plateau. *Annual Review of Earth and Planetary*  
486 *Sciences*, **38**(1): 77-102.
- 487 Nan, S. L., P. Zhao, and S. Yang, 2009: Springtime tropospheric temperature over the Tibetan Plateau  
488 and evolution of the tropical Pacific SST. *J. Geophys. Res.*, **114**, D10104.
- 489 Park, H. S., J. C. Chiang, S. Bordoni, 2012: The mechanical impact of the Tibetan Plateau on the  
490 seasonal evolution of the South Asian monsoon. *J. Clim.*, **25**(7): 2394-2407.
- 491 Parsons, L. A., J. Yin, J. T. Overpeck, et al., 2014: Influence of the Atlantic Meridional Overturning  
492 Circulation on the monsoon rainfall and carbon balance of the American tropics. *Geophysical*  
493 *Research Letters*, **41**(1): 146-151.
- 494 Pascale, S., L. M. V. Carvalho, D. K. Adams, et al., 2019: Current and Future Variations of the  
495 Monsoons of the Americas in a Warming Climate. *Current Climate Change Reports*, **5**(3):  
496 125-144.
- 497 Prell, W. L., J. E. Kutzbach, 1992: Sensitivity of the Indian monsoon to forcing parameters and  
498 implications for its evolution. *Nature*, **360**(6405): 647-652.
- 499 Prell, W. L., J. E. Kutzbach, 1992: Sensitivity of the Indian monsoon to forcing parameters and  
500 implications for its evolution. *Nature*, **360**(6405): 647-652.
- 501 Quade, J., T. E. Cerling, J. R. Bowman, 1989: Development of Asian monsoon revealed by marked  
502 ecological shift during the latest Miocene in northern Pakistan. *Nature*, **342**(6246): 163-166.
- 503 Rossby, C. G., 1939: Relation between variations in the intensity of the zonal circulation of the  
504 atmosphere and the displacements of the semi-permanent centers of action. *J. Mar. Res.*, **2**:38-55.
- 505 Su, B., D. Jiang, R. Zhang, et al., 2018: Difference between the North Atlantic and Pacific meridional  
506 overturning circulation in response to the uplift of the Tibetan Plateau. *Climate of the Past*, **14**(6):  
507 751-762.

- 508 Tang, H., A. Micheels, J. T. Eronen, et al., 2013: Asynchronous responses of East Asian and Indian  
509 summer monsoons to mountain uplift shown by regional climate modelling experiments. *Clim.*  
510 *Dyn.*, **40**(5): 1531-1549.
- 511 Wang, B., J. Liu, H. J. Kim, et al., 2012: Recent change of the global monsoon precipitation  
512 (1979-2008). *Clim. Dyn.*, **39**(5): 1123-1135.
- 513 Wang, B., M. Biasutti, M. P. Byrne, et al., 2021: Monsoons climate change assessment. *Bulletin of the*  
514 *American Meteorological Society*, **102**(1): E1-E19.
- 515 Wang, B., Q. Ding, 2008: Global Monsoon: Dominant Mode of Annual Variation in the Tropics.  
516 *Dynamics of Atmospheres and Oceans*, **44**(3-4): 165-183.
- 517 Wang, C., L. Zhang, S. K. Lee, L. Wu, C. R. Mechoso, 2014: A global perspective on CMIP5 climate  
518 model biases. *Nat. Clim. Change*, **4**, 201-205.
- 519 Wang, Z., S. Yang, A. Duan, et al., 2019: Tibetan Plateau heating as a driver of monsoon rainfall  
520 variability in Pakistan. *Clim. Dyn.*, **52**(9): 6121-6130.
- 521 Webster, P. J., V. O. Magana, et al., 1998: Monsoons: processes, predictability, and the prospects for  
522 prediction. *J. Geophys. Res.*, **103**:14451-14510.
- 523 Wen, Q., J. Yao, K. Döös, et al., 2018: Decoding hosing and heating effects on global temperature and  
524 meridional circulations in a warming climate. *J. Clim.*, **31**(23): 9605-9623.
- 525 Wen, Q., H. Yang, 2020: Investigating the role of the Tibetan Plateau in the formation of Pacific  
526 meridional overturning circulation. *J. Clim.*, **33**(9): 3603-3617.
- 527 Wen, Q., K. Döös, Z. Lu, et al., 2020: Investigating the Role of the Tibetan Plateau in ENSO Variability.  
528 *J. Clim.*, **33**(11): 4835-4852.
- 529 Wu, G., Y. Liu, B. Dong, et al., 2012: Revisiting Asian monsoon formation and change associated with  
530 Tibetan Plateau forcing: I. Formation. *Clim. Dyn.*, **39**(5): 1169-1181.
- 531 Xie, S. P., C. Deser, G. A. Vecchi, et al., 2010: Global warming pattern formation: Sea surface  
532 temperature and rainfall. *J. Clim.*, **23**(4): 966-986.

- 533 Yang, H., Q. Wen, J. Yao, et al., 2017: Bjerknnes compensation in meridional heat transport under  
534 freshwater forcing and the role of climate feedback. *J. Clim.*, **30**(14): 5167-5185.
- 535 Yang, H., Q. Wen, 2020: Investigating the role of the Tibetan Plateau in the formation of Atlantic  
536 meridional overturning circulation. *J. Clim.*, **33**(9): 3585-3601.
- 537 Yim, S. Y., B. Wang, J. Liu, et al., 2014: A comparison of regional monsoon variability using monsoon  
538 indices. *Clim. Dyn.*, **43**(5-6): 1423-1437.
- 539 Zhang, K. X., G. C. Wang, J. L. Ji, et al., 2010: Paleogene-Neogene stratigraphic realm and  
540 sedimentary sequence of the Qinghai-Tibet Plateau and their response to uplift of the plateau.  
541 *Science China Earth Sciences*, **53**(9): 1271-1294.
- 542 Zhang, W., T. Zhou, and L. Zhang, 2017: Wetting and greening Tibetan Plateau in early summer in  
543 recent decades. *J. Geophys. Res.*, **122**, 5808-5822.
- 544 Zhao, P., Y. Zhu, and R. Zhang, 2007: An Asian-Pacific teleconnection in summer tropospheric  
545 temperature and associated Asian climate variability. *Climate Dyn.*, **29**, 293-303.
- 546 Zhao, P., B. Wang, J. Liu, et al., 2016: Summer precipitation anomalies in Asia and North America  
547 induced by Eurasian non-monsoon land heating versus ENSO. *Scientific reports*, **6**(1): 1-8.
- 548 Zhao, P., S. Yang, R. Wu, Z. Wen, J. Chen, and H. Wang, 2012: Asian origin of interannual variations  
549 of summer climate over the extratropical North Atlantic Ocean. *J. Clim.*, **25**, 6594-6609.

550

551

552

553

554

555

556

557

## Figure Captions

558 **Figure 1** Topography configuration (units: m) for (a) CTRL and (b) NoTP.

559 **Figure 2** (a) Time evolution of percentage changes in Atlantic meridional overturning circulation  
560 (AMOC) with light blue curves representing results from 10 ensemble fully coupled runs. The  
561 AMOC index is defined as the maximum streamfunction in the range of  $0^{\circ}$ – $10^{\circ}$ C over  $20^{\circ}$ – $70^{\circ}$ N in  
562 the Atlantic. (b) Equilibrium changes in geopotential height (shading; m) and wind (vector; m/s)  
563 at 850 hPa during boreal summer in SOM runs. (c) Equilibrium changes in surface air temperature  
564 (SAT;  $^{\circ}$ C) during boreal summer in SOM runs. (d) and (e) are the same as (b) and (c), but for fully  
565 coupled runs.

566 **Figure 3** (a) Time evolution of changes in North American summer monsoon (NASM) precipitation  
567 (mm/day). Blue curves are for precipitation change, with solid curve for fully coupled runs and  
568 dashed curve for SOM runs. Red curves are for percentage changes in precipitation, with solid  
569 curve for fully coupled runs and dashed curve for SOM runs. (b) Equilibrium changes in  
570 precipitation (mm/day) during boreal summer in SOM runs. (c) Equilibrium changes in surface  
571 humidity (shading; g/kg) during boreal summer in SOM runs with mean values (purple contours;  
572 g/kg) from CTRL\_SOM. (d) and (e) are the same as (b) and (c) but for fully coupled runs. In  
573 (b)-(e), the stippling areas indicate the difference exceeding 95% confidence level, determined by  
574 a two-tailed Student's t test. The black contours denote the North American monsoon region,  
575 which is defined as the region where the local summer precipitation minus local winter  
576 precipitation exceeding 2mm/day and the local summer precipitation exceeds 55% of annual  
577 rainfall in CTRL run. In (d), the purple contours denote the NAM region by using GPCP data  
578 from 1979-2018.

579 **Figure 4** Equilibrium changes in (a) precipitation ( $P'$ ), (b) evaporation ( $E'$ ), (c) thermodynamic  
580 component of vertical moisture advection ( $-\langle\omega q'\rangle$ ), (d) dynamic component of vertical moisture

581 advection ( $-\langle \omega' q \rangle$ ), **(e)** thermodynamic component of horizontal moisture advection ( $-\langle V \cdot \nabla q' \rangle$ ),  
 582 and **(f)** dynamic component of horizontal moisture advection ( $-\langle V' \cdot \nabla q \rangle$ ) in SOM runs during  
 583 boreal summer. Units: mm/day. The black contours denote the North American monsoon region.

584 **Figure 5** Same as Fig. 4 but for fully coupled runs. The black contours denote the North American  
 585 monsoon region.

586 **Figure 6** Bar chart for the mean changes in **(a)** precipitation and its contribution terms and **(b)**  
 587 dynamic component of vertical moisture advection and its contribution terms. Orange bar is for  
 588 SOM runs and blue bar is for fully coupled runs. In **(a)**, The meaning of labels at x-axis is the same  
 589 as that in Fig. 4. In **(b)**,  $-\omega_W' q$  denotes the dynamic term due to zonal circulation change and  
 590  $-\omega_H' q$  denotes the dynamic term due to meridional circulation change. Units: mm/day. All values  
 591 are from boreal summer.

592 **Figure 7** Left panel is the annual mean state of vertical velocity (units: Pa/s) at 500 hPa in **(a)** CTRL,  
 593 **(b)** NoTP, **(c)** CTRL\_SOM, and **(d)** CTRL\_NoTP. Right panel is the same as left panel but for  
 594 boreal summer. Positive value is for upward motion. The black contours denote the North  
 595 American monsoon region.

596 **Figure 8** Left panel is the annual mean state of precipitation (units: mm/day) in **(a)** CTRL, **(b)** NoTP,  
 597 **(c)** CTRL\_SOM, and **(d)** CTRL\_NoTP. Right panel is the same as left panel but for boreal summer.  
 598 The black contours denote the North American monsoon region.

599 **Figure 9** **(a)** Total vertical velocity and its **(b)** meridional component, **(c)** zonal component and **(d)**  
 600 residual in CTRL\_SOM at 500 hPa during boreal summer. **(e)-(h)** are the same as **(a)-(d)** but for  
 601 CTRL. The decomposition are based on 3P-DGAC method. Units: Pa/s.

602 **Figure 10** Equilibrium changes in **(a)** total vertical velocity (units: Pa/s) and its **(b)** meridional  
603 component and **(c)** zonal component at 500 hPa during boreal summer in SOM runs, respectively.  
604 **(d)-(f)** are the same as **(a)-(c)** but for fully coupled runs. The red rectangle outlines the eastern  
605 Pacific-Atlantic section.

606 **Figure 11** Mass stream function ( $10^{11}$ kg/s) averaged between  $120^{\circ}$ W and  $20^{\circ}$ W during boreal  
607 summer in **(a)** SOM runs and **(c)** fully coupled runs. The black contours denote the mean values  
608 in a world with TP while the shadings denote the difference. **(b)** and **(d)** are the vertical averaged  
609 mass stream function in **(a)** and **(c)** correspondingly.

610 **Figure 12** **(a)** Equilibrium changes in zonal mean precipitation (mm/day; red curve) and SAT ( $^{\circ}$ C;  
611 dashed black curve) during boreal summer over the eastern Pacific-Atlantic section in SOM runs.  
612 **(b)** Equilibrium changes in precipitation (mm/day; shading) and the location of Intertropical  
613 Convergence Zone (ITCZ) during boreal summer in SOM runs. The green dots are for ITCZ in a  
614 world without the TP while the black dots are for ITCZ in a world with the TP. **(c)-(d)** are the  
615 same as **(a)-(b)** but for fully coupled runs.

616 **Figure 13** **(a)** Changes in net atmospheric energy input during boreal summer between CTRL and  
617 NoTP. **(b)** Same as **(a)** but only shows the TOA component. **(c)** Same as **(a)** but only shows the  
618 surface component. Units:  $\text{W}/\text{m}^2$ . **(d)** Changes in the divergent meridional component of the  
619 atmospheric energy transport (AET) during boreal summer in fully coupled runs. Units:  $10^7\text{W}/\text{m}$ .  
620 The red arrow represents the southward transport of AET. The calculation for AET follows  
621 Mamalakis et al (2021).

## Figures

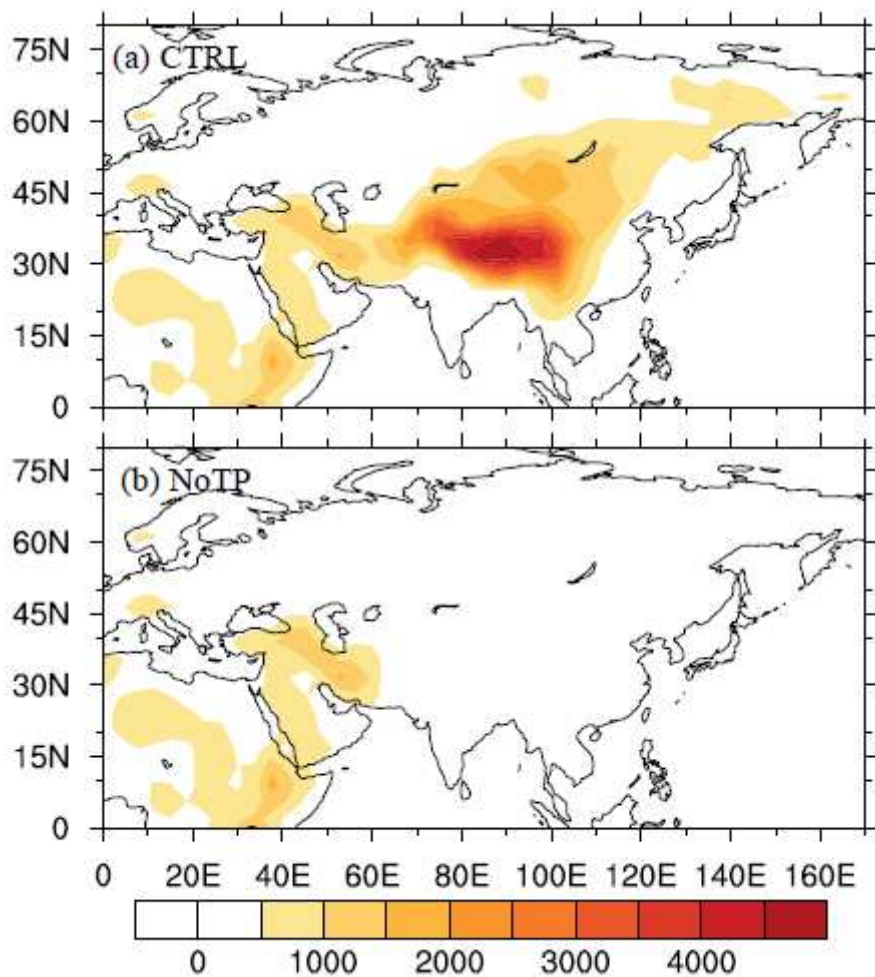


**Figure 1**

Topography configuration (units: m) for (a) CTRL and (b) NoTP. Note: The designations employed and the presentation of the material on this map do not imply the expression of any opinion whatsoever on the part of Research Square concerning the legal status of any country, territory, city or area or of its authorities, or concerning the delimitation of its frontiers or boundaries. This map has been provided by the authors.

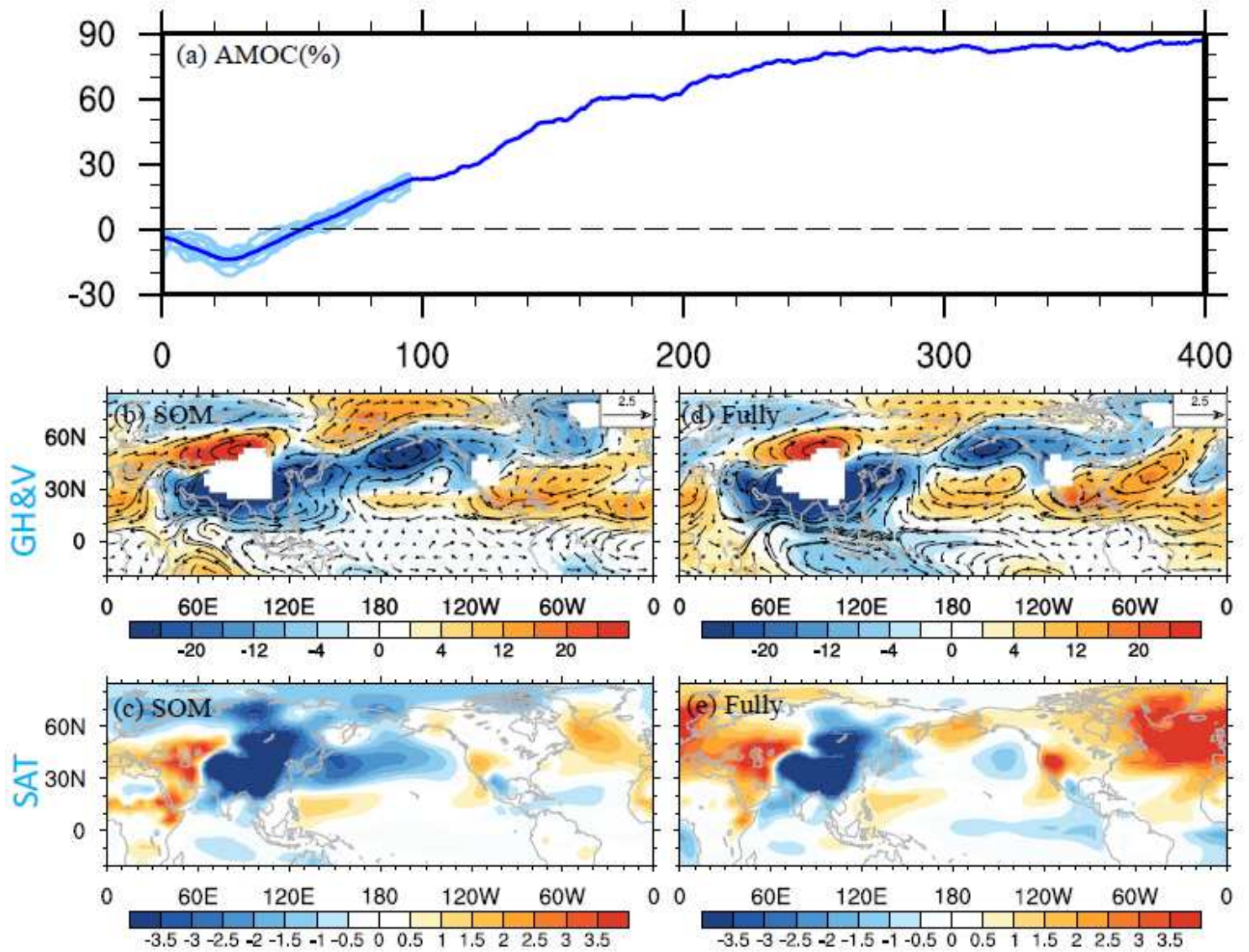


**Figure 2**

(a) Time evolution of percentage changes in Atlantic meridional overturning circulation (AMOC) with light blue curves representing results from 10 ensemble fully coupled runs. The AMOC index is defined as the maximum streamfunction in the range of  $0^{\circ}$ – $10^{\circ}$ C over  $20^{\circ}$ – $70^{\circ}$ N in the Atlantic. (b) Equilibrium changes in geopotential height (shading; m) and wind (vector; m/s) at 850 hPa during boreal summer in SOM runs. (c) Equilibrium changes in surface air temperature (SAT;  $^{\circ}$ C) during boreal summer in SOM runs. (d) and (e) are the same as (b) and (c), but for fully coupled runs. Note: The designations employed and the presentation of the material on this map do not imply the expression of any opinion whatsoever on the part of Research Square concerning the legal status of any country, territory, city or area or of its authorities, or concerning the delimitation of its frontiers or boundaries. This map has been provided by the authors.

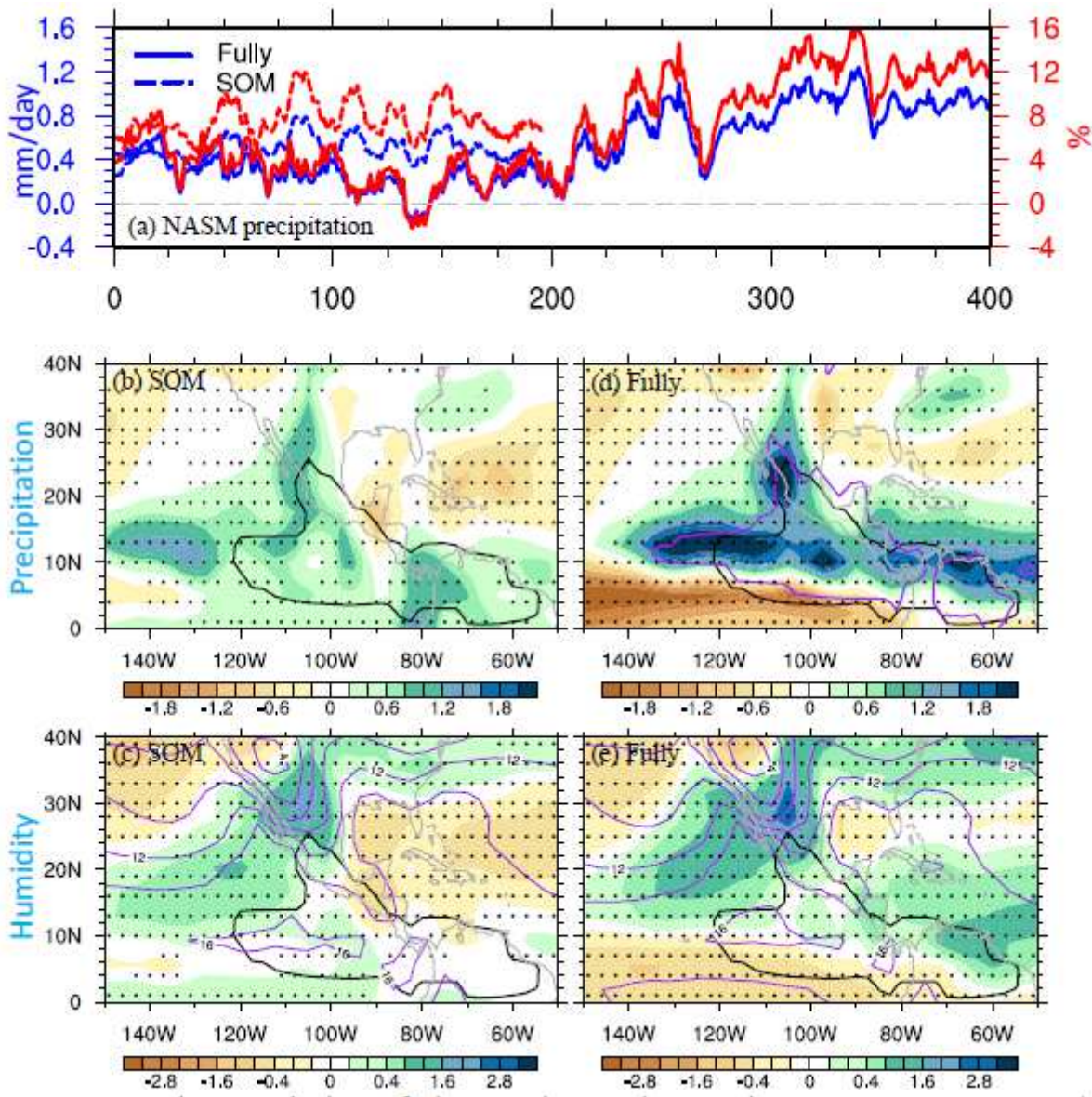


**Figure 3**

(a) Time evolution of changes in North American summer monsoon (NASM) precipitation (mm/day). Blue curves are for precipitation change, with solid curve for fully coupled runs and dashed curve for SOM runs. Red curves are for percentage changes in precipitation, with solid curve for fully coupled runs and dashed curve for SOM runs. (b) Equilibrium changes in precipitation (mm/day) during boreal summer in SOM runs. (c) Equilibrium changes in surface humidity (shading; g/kg) during boreal summer in SOM runs with mean values (purple contours; g/kg) from CTRL\_SOM. (d) and (e) are the same as (b) and (c) but for fully coupled runs. In (b)-(e), the stippling areas indicate the difference exceeding 95% confidence level, determined by a two-tailed Student's t test. The black contours denote the North American monsoon region, which is defined as the region where the local summer precipitation minus local winter precipitation exceeding 2mm/day and the local summer precipitation exceeds 55% of annual rainfall in CTRL run. In (d), the purple contours denote the NAM region by using GPCP data from 1979-2018.

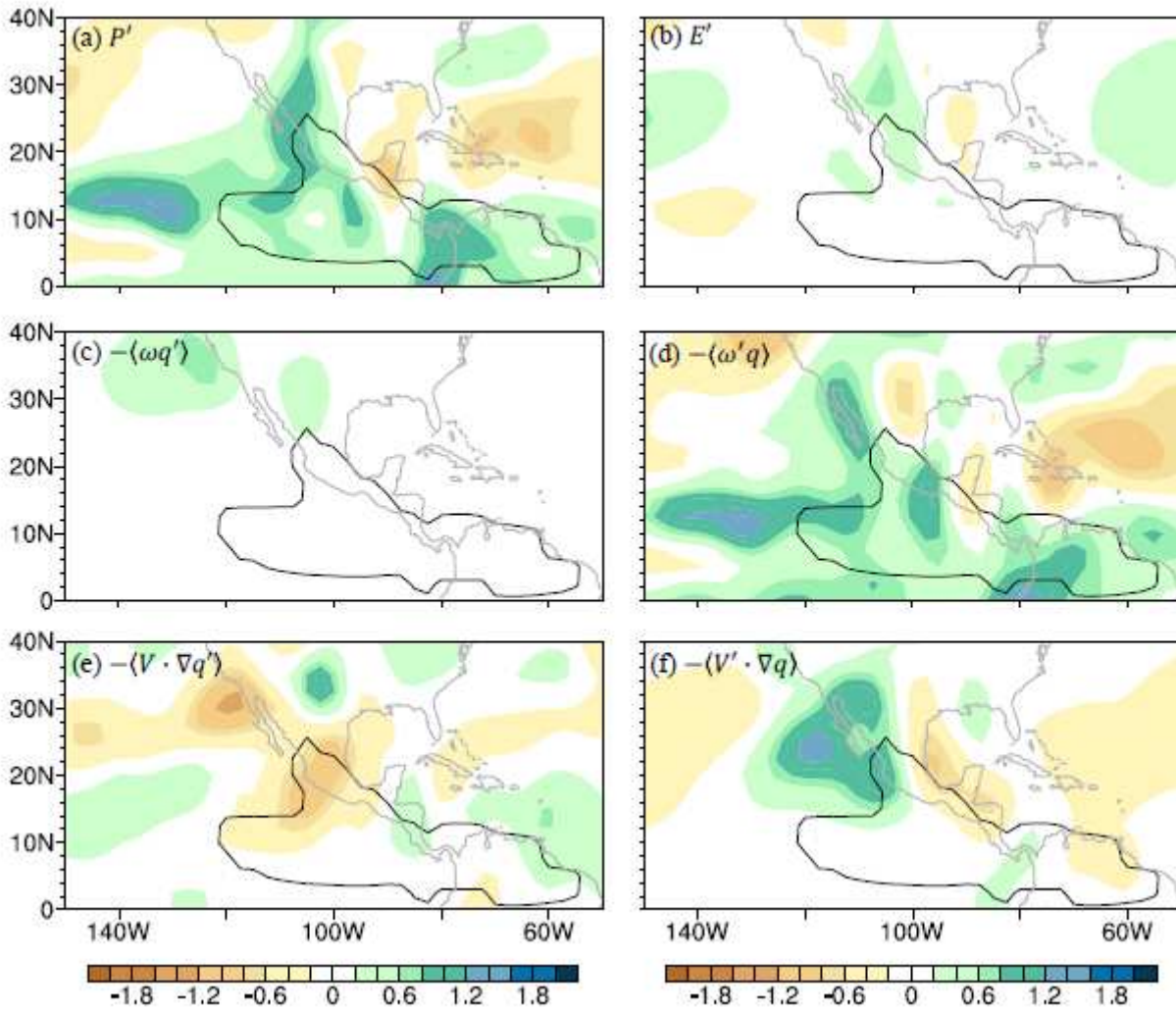


**Figure 4**

Equilibrium changes in (a) precipitation ( $P'$ ), (b) evaporation ( $E'$ ), (c) thermodynamic component of vertical moisture advection ( $-\langle \omega q' \rangle$ ), (d) dynamic component of vertical moisture advection ( $-\langle \omega' q \rangle$ ), (e) thermodynamic component of horizontal moisture advection ( $-\langle V \cdot \nabla q' \rangle$ ), and (f) dynamic component of horizontal moisture advection ( $-\langle V' \cdot \nabla q \rangle$ ) in SOM runs during boreal summer. Units: mm/day. The black contours denote the North American monsoon region.

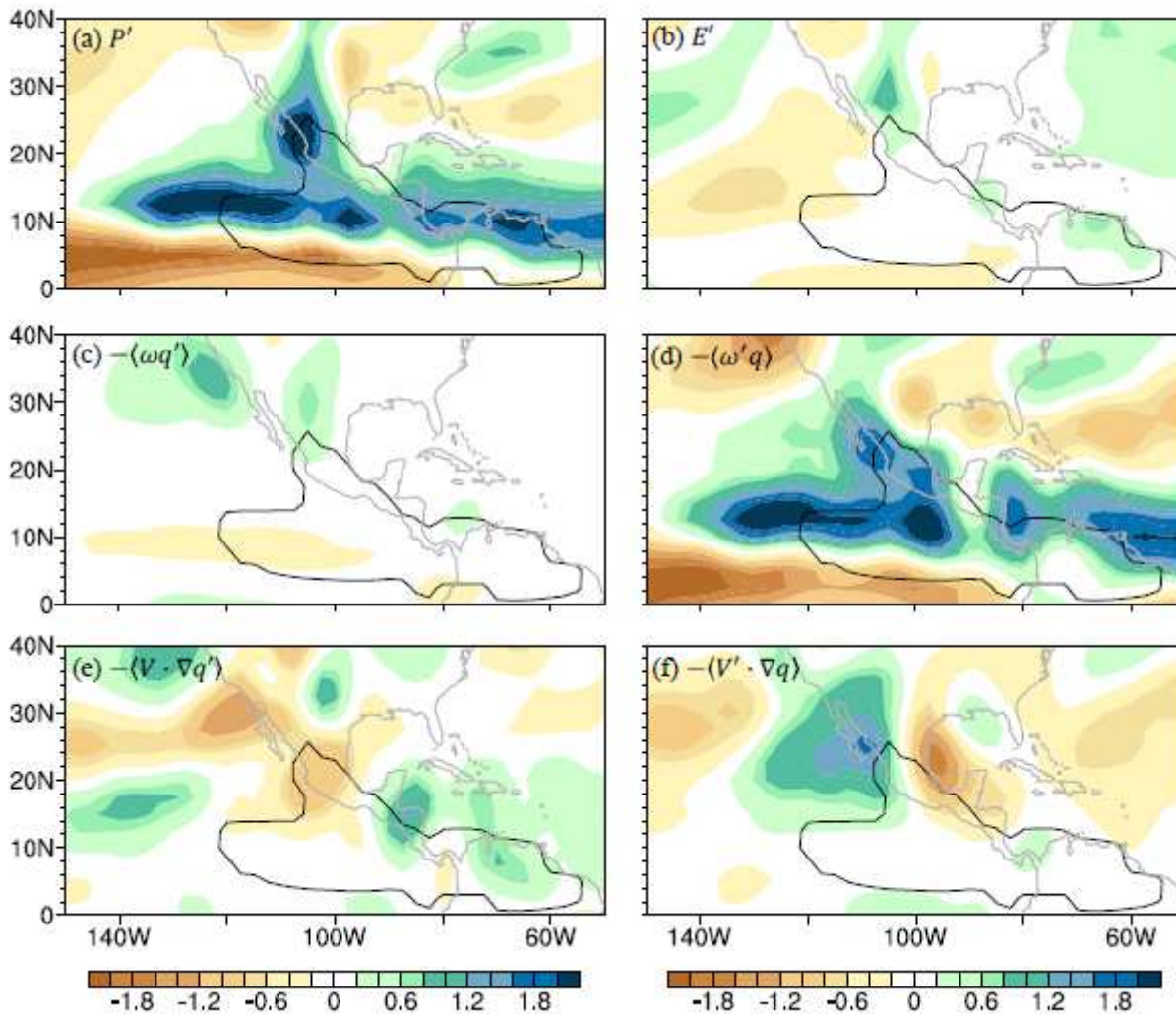


**Figure 5**

Same as Fig. 4 but for fully coupled runs. The black contours denote the North American monsoon region.

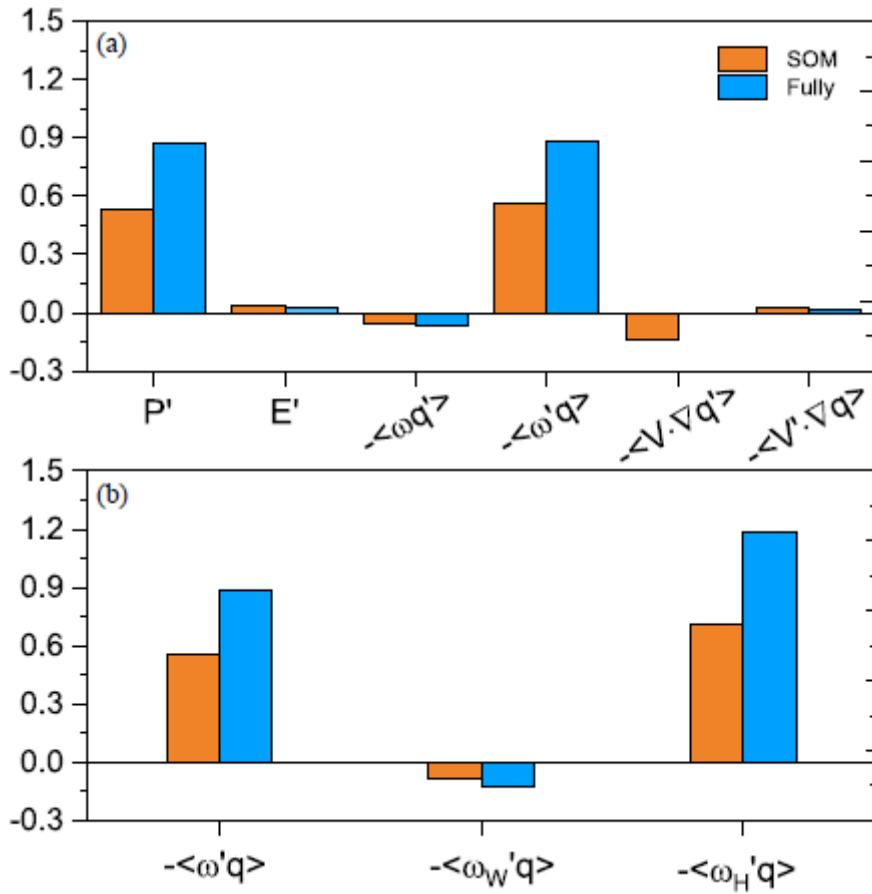


**Figure 6**

Bar chart for the mean changes in (a) precipitation and its contribution terms and (b) dynamic component of vertical moisture advection and its contribution terms. Orange bar is for SOM runs and blue bar is for fully coupled runs. In (a), The meaning of labels at x-axis is the same as that in Fig. 4. In (b),  $-\omega_W'q$  denotes the dynamic term due to zonal circulation change and  $-\omega_H'q$  denotes the dynamic term due to meridional circulation change. Units: mm/day. All values are from boreal summer.

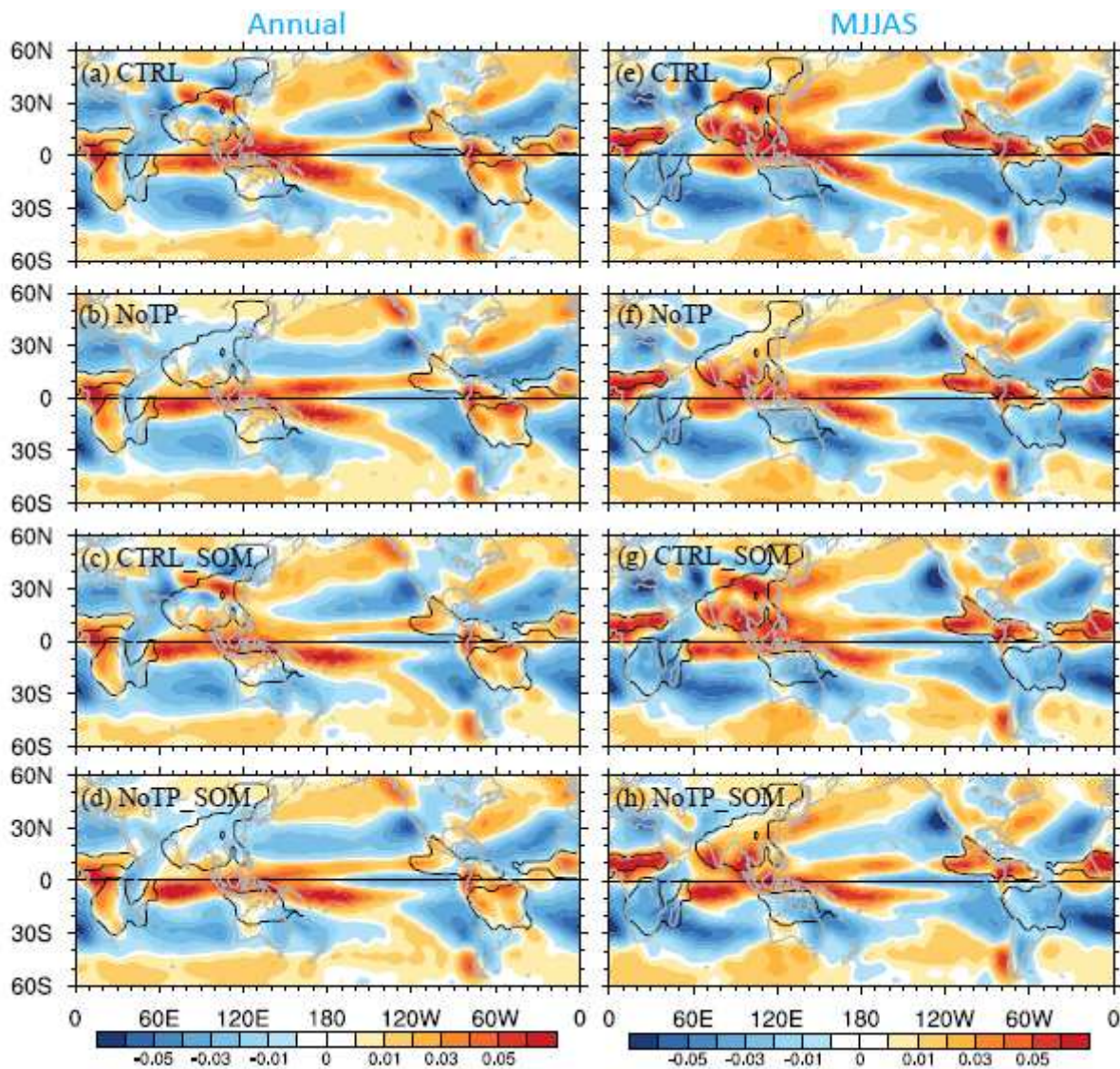


**Figure 7**

Left panel is the annual mean state of vertical velocity (units: Pa/s) at 500 hPa in (a) CTRL, (b) NoTP, (c) CTRL\_SOM, and (d) CTRL\_NoTP. Right panel is the same as left panel but for boreal summer. Positive value is for upward motion. The black contours denote the North American monsoon region. Note: The designations employed and the presentation of the material on this map do not imply the expression of any opinion whatsoever on the part of Research Square concerning the legal status of any country, territory, city or area or of its authorities, or concerning the delimitation of its frontiers or boundaries. This map has been provided by the authors.

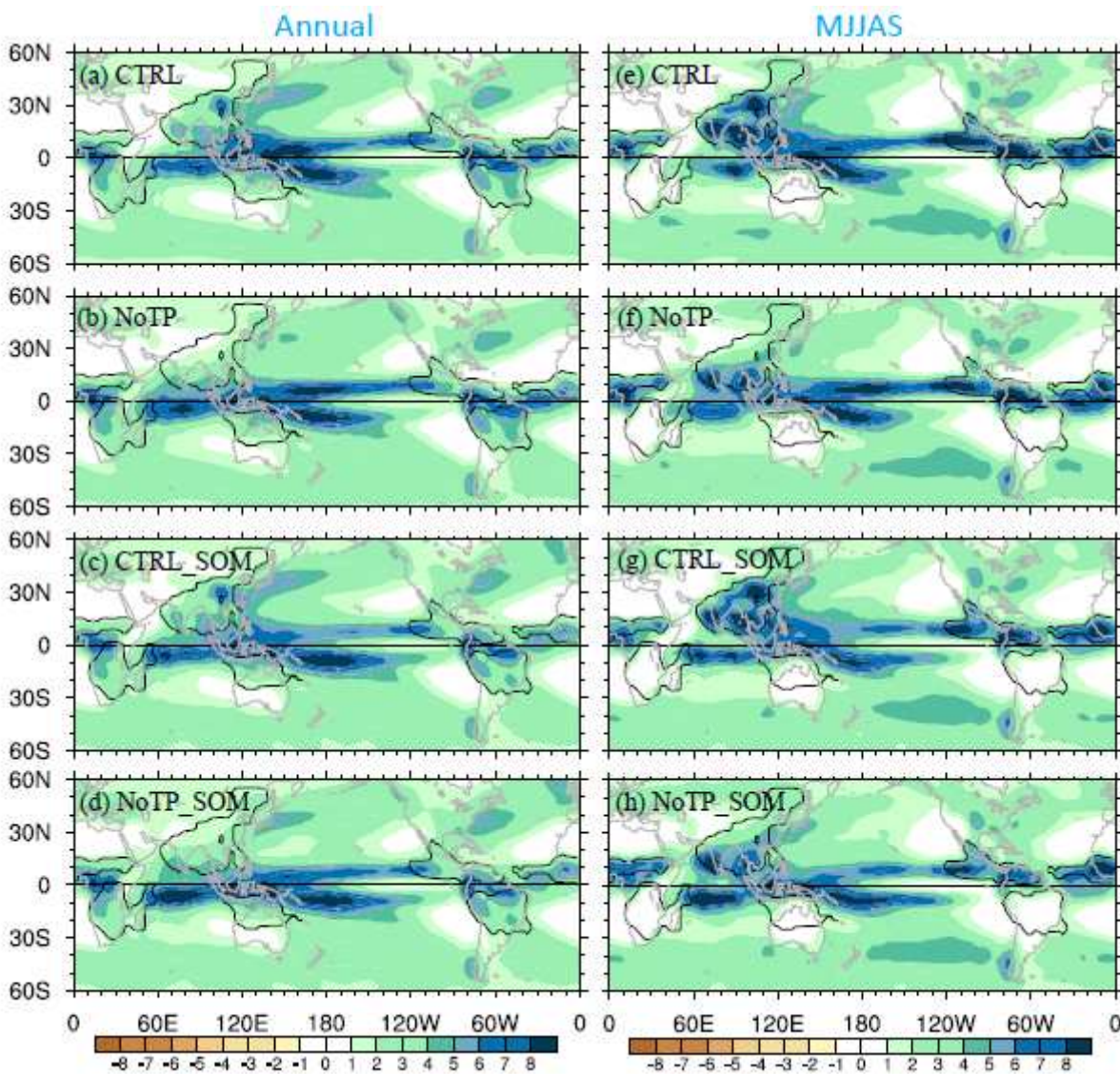


**Figure 8**

Left panel is the annual mean state of precipitation (units: mm/day) in (a) CTRL, (b) NoTP, (c) CTRL\_SOM, and (d) CTRL\_NoTP. Right panel is the same as left panel but for boreal summer. The black contours denote the North American monsoon region. Note: The designations employed and the presentation of the material on this map do not imply the expression of any opinion whatsoever on the part of Research Square concerning the legal status of any country, territory, city or area or of its authorities, or concerning the delimitation of its frontiers or boundaries. This map has been provided by the authors.

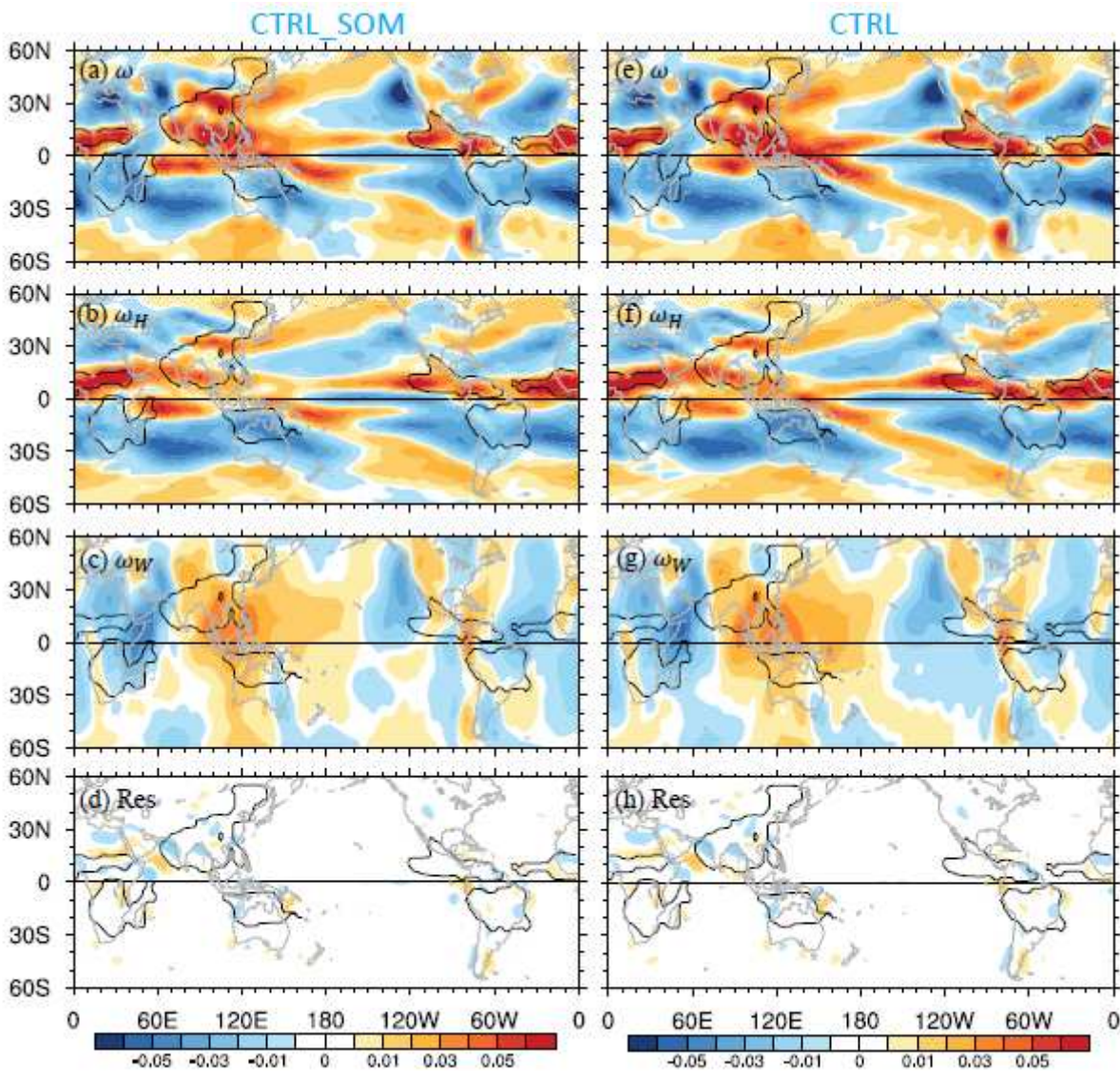


**Figure 9**

(a) Total vertical velocity and its (b) meridional component, (c) zonal component and (d) residual in CTRL\_SOM at 500 hPa during boreal summer. (e)-(h) are the same as (a)-(d) but for CTRL. The decomposition are based on 3P-DGAC method. Units: Pa/s. Note: The designations employed and the presentation of the material on this map do not imply the expression of any opinion whatsoever on the part of Research Square concerning the legal status of any country, territory, city or area or of its authorities, or concerning the delimitation of its frontiers or boundaries. This map has been provided by the authors.

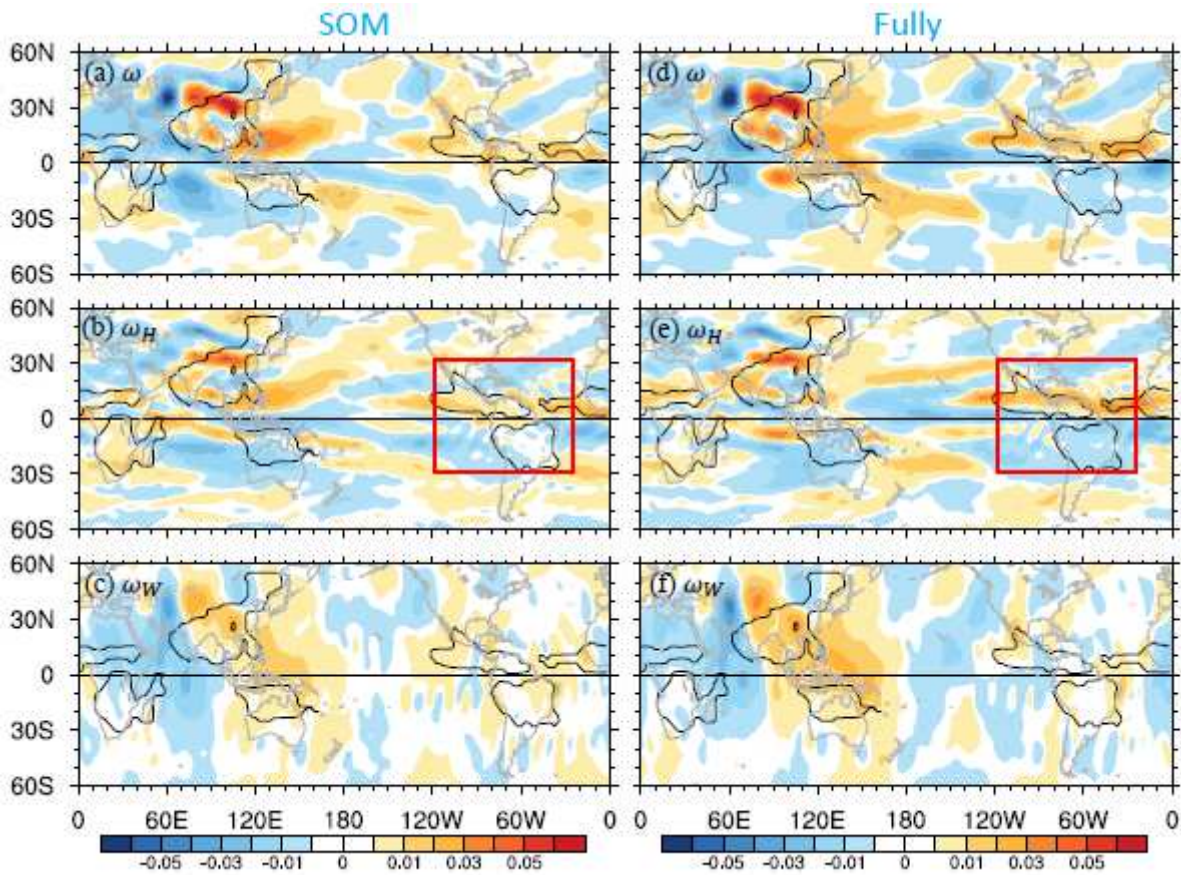


**Figure 10**

Equilibrium changes in (a) total vertical velocity (units: Pa/s) and its (b) meridional component and (c) zonal component at 500 hPa during boreal summer in SOM runs, respectively. (d)-(f) are the same as (a)-(c) but for fully coupled runs. The red rectangle outlines the eastern Pacific-Atlantic section. Note: The designations employed and the presentation of the material on this map do not imply the expression of any opinion whatsoever on the part of Research Square concerning the legal status of any country, territory, city or area or of its authorities, or concerning the delimitation of its frontiers or boundaries. This map has been provided by the authors.

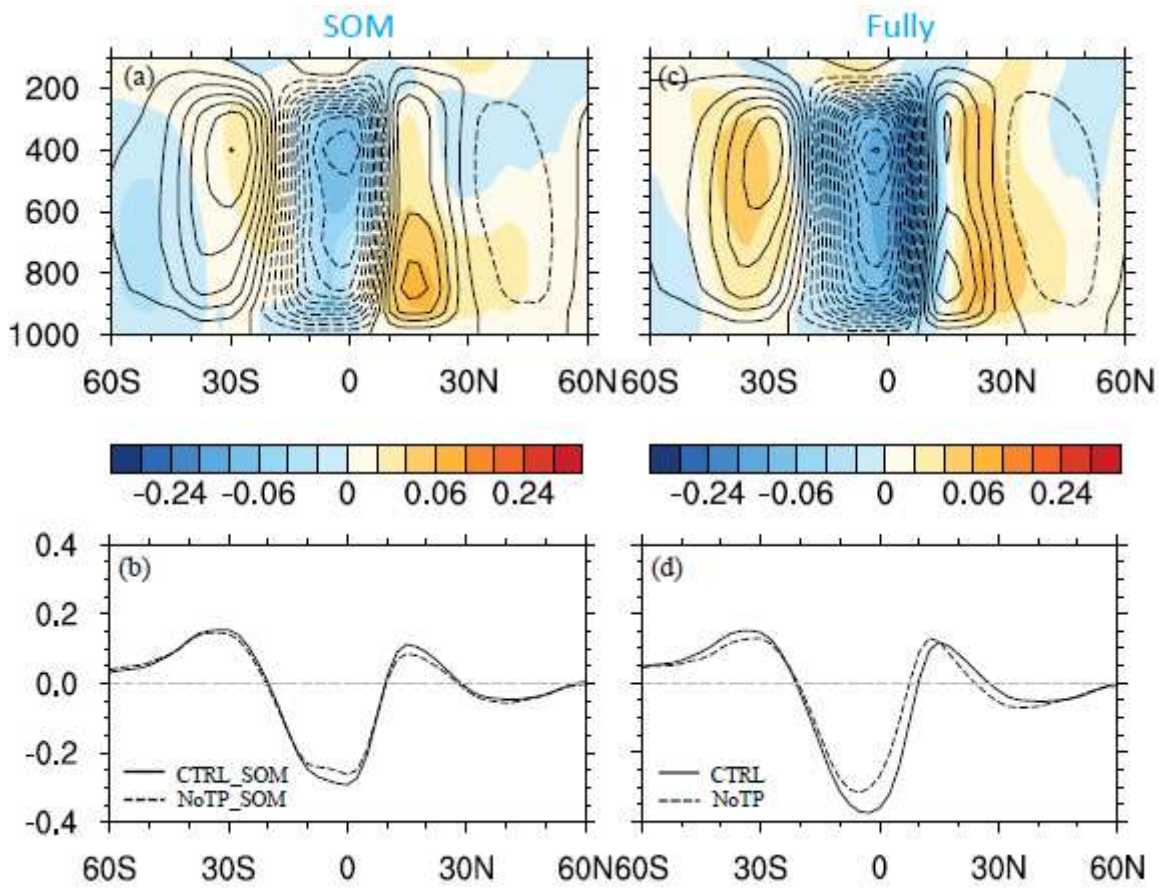


Figure 11

Mass stream function ( $10^{11} \text{kg/s}$ ) averaged between  $120^\circ\text{W}$  and  $20^\circ\text{W}$  during boreal summer in (a) SOM runs and (c) fully coupled runs. The black contours denote the mean values in a word with TP while the shadings denote the difference. (b) and (d) are the vertical averaged mass stream function in (a) and (c) correspondingly.

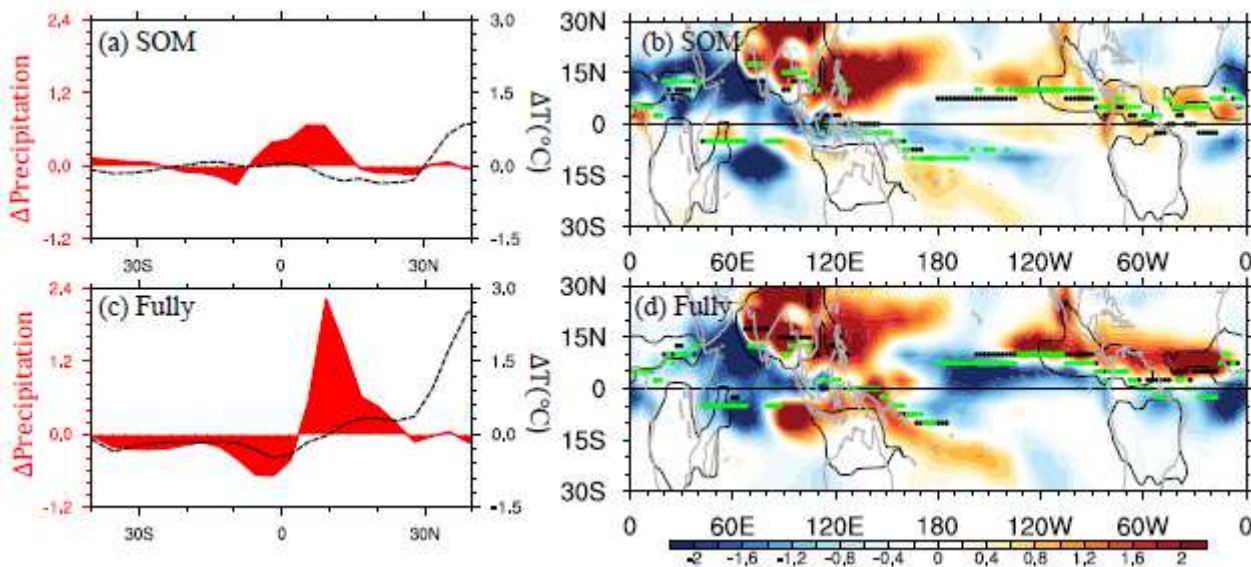
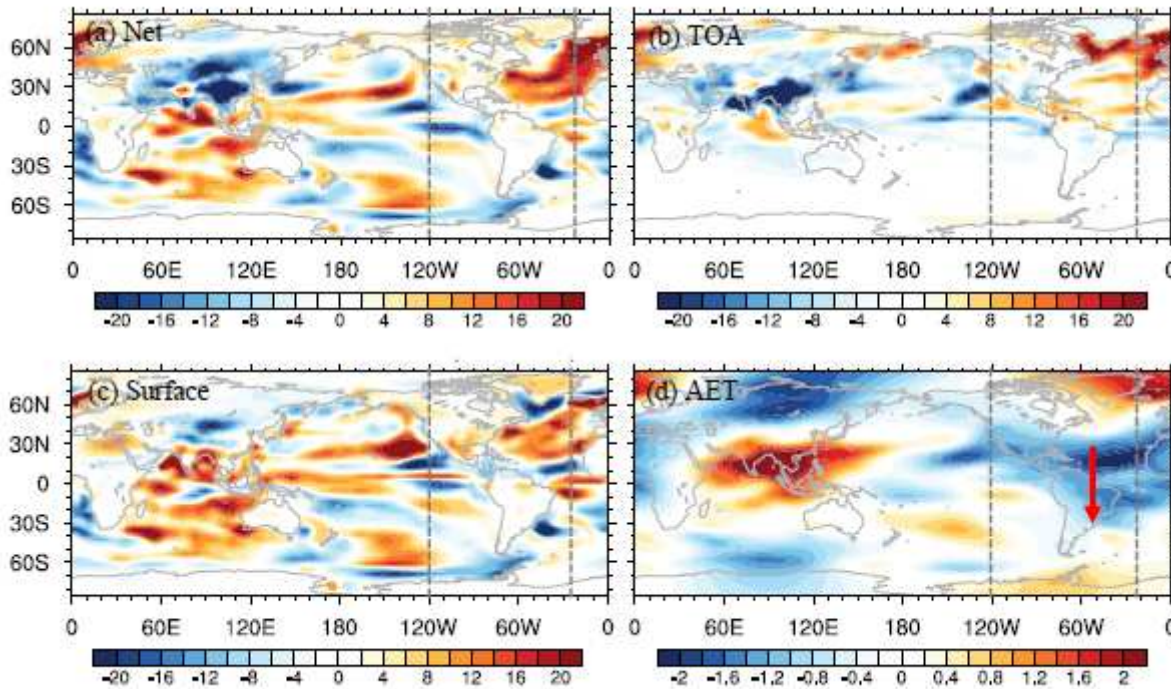


Figure 12

(a) Equilibrium changes in zonal mean precipitation (mm/day; red curve) and SAT (oC; dashed black curve) during boreal summer over the eastern Pacific-Atlantic section in SOM runs. (b) Equilibrium changes in precipitation (mm/day; shading) and the location of Intertropical Convergence Zone (ITCZ) during boreal summer in SOM runs. The green dots are for ITCZ in a world without the TP while the black dots are for ITCZ in a world with the TP. (c)-(d) are the same as (a)-(b) but for fully coupled runs. Note: The designations employed and the presentation of the material on this map do not imply the expression of any opinion whatsoever on the part of Research Square concerning the legal status of any country, territory, city or area or of its authorities, or concerning the delimitation of its frontiers or boundaries. This map has been provided by the authors.



**Figure 13**

(a) Changes in net atmospheric energy input during boreal summer between CTRL and NoTP. (b) Same as (a) but only shows the TOA component. (c) Same as (a) but only shows the surface component. Units: W/m<sup>2</sup>. (d) Changes in the divergent meridional component of the atmospheric energy transport (AET) during boreal summer in fully coupled runs. Units: 10<sup>7</sup>W/m. The red arrow represents the southward transport of AET. The calculation for AET follows Mamalakis et al (2021). Note: The designations employed and the presentation of the material on this map do not imply the expression of any opinion whatsoever on the part of Research Square concerning the legal status of any country, territory, city or area or of its authorities, or concerning the delimitation of its frontiers or boundaries. This map has been provided by the authors.